A self-consistent formulation for the sensitivity analysis of finite amplitude vortex shedding in the cylinder wake

P. Meliga[1], E. Boujo[2] and F. Gallaire[2]

[1] Aix-Marseille Université, CNRS, Ecole Centrale Marseille, Laboratoire M2P2, Marseille, France

[2] LFMI, École Polytechnique Fédérale de Lausanne, CH-1015 Lausanne, Switzerland

(Received ?; revised ?; accepted ?. - To be entered by editorial office)

We use the adjoint method to compute sensitivity maps for the limit-cycle frequency and amplitude of the Bénard-von Kármán vortex street in the wake of a circular cylinder. The sensitivity analysis is performed in the frame of the semi-linear self-consistent model recently introduced by Mantič *et al.* (Phys. Rev. Lett. 2014; vol.113; 084501), which allows to describe accurately the effect of the control on the mean flow, but also on the finite-amplitude fluctuation that couples back nonlinearly onto the mean flow via the formation of Reynolds stress. The sensitivity is computed with respect to arbitrary steady and synchronous time-harmonic body forces. For small amplitude of the control, the theoretical variations of the limit-cycle frequency predict well those of the controlled flow, as obtained from either self-consistent modeling or direct numerical simulation of the Navier–Stokes equations. This is not the case if the variations are computed in the simpler mean flow approach overlooking the coupling between the mean and fluctuating components of the flow perturbation induced by the control. The variations of the limit-cycle amplitude (that falls out the scope of the mean flow approach) are also correctly predicted, meaning that the approach can serve as a relevant and systematic guideline

to control strongly unstable flows exhibiting non-small, finite amplitudes of oscillation. As an illustration, we apply the method to control by means of a small secondary control cylinder and discuss the obtained results in the light of the seminal experiments of Strykowski & Sreenivasan (J. Fluid Mech. 1990; vol. 218; pp. 71-107).

---

1. Introduction

The vortex shedding instability leading to the Bénard-von Kármán vortex street in the wake of a circular cylinder is a well-known example of hydrodynamic limit cycle: above the critical Reynolds number $Re_c = 47$ (built from the free stream velocity and the cylinder diameter), a self-sustained pattern of regularly alternated vortices is shed at a well-defined frequency. This instability is very robust and the essentially periodic nature of vortex shedding persists up to the turbulent regime (Williamson 1996).

An interesting feature of this instability is that, except in the very vicinity of the threshold, the main space and time properties of the flow oscillations (frequency, amplitude) cannot be captured by classical linear and weakly nonlinear analyses performed on the base flow (i.e., the steady solution of the Navier–Stokes equations (NSE) that becomes unstable at Re_c). For instance, Barkley (2006) shows that the frequency prediction issuing from a linear global stability analysis fails by a large amount, even at Reynolds numbers as low as $Re = 80$. In the same fashion, the Stuart–Landau amplitude equation describing the onset of limit-cycle oscillations, albeit derived rigorously from the NSE using a multiple-scale expansion (Stuart 1960, see also Sipp & Lebedev 2007; Meliga *et al.* 2009*a*, 2012*a* for an application to spatially developing flows) fails to provide correct amplitude and frequency corrections at Reynolds numbers above the bifurcation threshold by only 10%. This is because these approaches are perturbative in nature, and

build all oscillating fields as successive-order corrections to the eigenmode feeding on the neutrally stable base flow, whose spatial structure differs considerably from that of the saturated nonlinear oscillation (Dušek *et al.* 1994; Noack *et al.* 2003).

Barkley (2006) reports that a linear global stability analysis can still satisfactorily predict the shedding frequency well above the instability threshold provided it is performed on the time-averaged mean flow, not the base flow. This is somehow reminiscent of Hammond & Redekopp (1997) and Pier (2002), who early noticed that a linear criterion applied to the mean flow was remarkably successful in predicting the frequency of the unsteadiness in the frame of local stability analyses. In addition, Barkley (2006) shows that the mean flow is almost neutrally stable. Such results have been rationalized by Sipp & Lebedev (2007) analyzing the nonlinear interactions contributing to the Landau coefficient of the amplitude equation. The authors conclude that (i) the mean flow being neutrally stable and (ii) its eigenfrequency being a good predictor of the nonlinear frequency are due to the fact that base flow modifications dominate the flow nonlinearity over the generation of higher harmonics, which produces close-to-harmonic oscillations. This can be seen as a theoretical proof, valid in the vicinity of the instability threshold, of the general picture used to describe the mechanism for nonlinear saturation in the cylinder wake and related flows : perturbations feed on the unstable base flow, grow, modify the base flow via the formation of Reynolds stress, which in turn reduces their growth rate up to the point where it becomes zero. At this stage, the unstable base flow has been distorted into the neutrally stable mean flow, and perturbations stop growing and saturate (Maurel *et al.* 1995; Zielinska *et al.* 1997). Note, this idea of an instability saturating itself through nonlinear terms leading to a neutrally stable mean flow has been early formulated by Malkus (1956) in the context of turbulent flows.

Several studies have recently aimed at taking into account this distortion of the base

flow via Reynolds stress modeled averaging the products of single eigenmode disturbances (Farrell & Ioannou 2012; Pralits *et al.* 2015 and the references therein). Of particular interest is the semi-linear model introduced by Mantič-Lugo *et al.* (2014) to capture the finite-amplitude saturation of the shedding instability. This model is derived rigorously from the Reynolds decomposition of the NSE under the assumption that the nonlinearity reduces to the production of mean flow modifications. The fluctuation is modeled as the leading global eigenmode satisfying the NSE linearized about the mean flow, while the mean flow is obtained as a steady solution of the NSE forced by the Reynolds stress of the eigenmode (hence the semi-linearity, not to be confused with the semi-linear terminology used to classify partial differential equations). This sets up a self-consistent description of the mean flow/fluctuation interaction, both problems being coupled nonlinearly and to be solved simultaneously. For given Reynolds number, the sole free parameter is the amplitude of the eigenmode, which for a specific value leads to a neutrally stable mean flow: this is the saturation amplitude of the model, that yields a definite approximation of the mean flow, of the fluctuation and of the oscillation frequency. Comparison with direct numerical simulations (DNS) have established that the model captures accurately the frequency and saturation amplitude of the instability up to Reynolds number $Re \sim 100$.

In a seminal experiment, Strykowski & Sreenivasan (1990) investigate experimentally the flow around a circular cylinder perturbed by a smaller circular cylinder positioned in the near wake. For various Reynolds numbers and diameter ratios of the two cylinders, they measure the influence of this secondary control cylinder in terms of sensitivity maps showing the regions around the main cylinder where shedding is most affected. For specific locations, Strykowski & Sreenivasan (1990) report a stabilization of the wake accompanied by a decrease of the shedding frequency that could go towards complete

suppression of unsteadiness. They also provide experimental evidence that suppression of vortex shedding is correlated with negative growth rates of the instability. Since then, the prohibitive cost of producing exhaustive sensitivity maps under traditional procedures - which requires systematical experimental measurements, or numerical simulations to be performed over large ranges of parameter spaces - has motivated the development of more systematical approaches relying on theoretical analysis to map quickly the best positions for placement of the control cylinder.

Hill (1992) has pioneered the use of Lagrangian-based adjoint methods to compute theoretical sensitivity maps capable of assessing (within one single calculation) the effect of given control upon the stability properties of the base flow. Hill (1992) models the presence of the control cylinder by a point-wise supply of momentum equal and opposite to the anticipated drag. He uses the adjoint method to compute the sensitivity of the unstable eigenmode (representing mathematically the variational derivative of its eigenvalue to a body force or a wall velocity), whereafter he ultimately retrieves the structure of the experimental sensitivity maps without ever having calculated the actual controlled states. Such an approach (herein referred to as the *base flow approach*) offers an attractive alternative to bottleneck "trial and error" procedures, as it allows exhaustive coverage of large parameter spaces at very low computational costs. It has sparked renewed interest in the last decade, through a substantial body of work focusing on steady and unsteady effects modeling the presence of the control cylinder (Giannetti & Luchini 2007; Marquet *et al.* 2008*a*), and is now routinely applied to a variety of flow configurations (Meliga *et al.* 2010; Pralits *et al.* 2010; Alizard *et al.* 2010) and control targets, including optimal transient growth and optimal harmonic response (Brandt *et al.* 2011; Boujo *et al.* 2013), recirculation length (Boujo & Gallaire 2014) or aerodynamic forces (Meliga *et al.* 2014).

Of course, the method is bound to fail if the stability analysis is not predictive for

the main features of the unsteadiness, hence the low Reynolds numbers ($Re \sim 47 - 60$) considered in Hill (1992) and other aforementioned studies. Another approach is thus needed to predict similarly how the control affects the finite-amplitude vortex shedding prevailing at Reynolds numbers well above the instability threshold. Meliga *et al.* (2012*b*) have proposed to analyze similarly the sensitivity of the mean flow stability properties, a so-called *mean flow approach* that has yielded promising results (Meliga *et al.* 2012*b*; Camarri *et al.* 2013; Meliga *et al.* 2014), but is not entirely satisfactory though : first, because its scope is limited to the vortex shedding frequency, as mean flow stability analyses do not predict the amplitude of the oscillation. Second, because it relies on a so-called frozen Reynolds stress modeling overlooking the effect of the control on the Reynolds stress. This one-way mean flow/fluctuation coupling (in the sense that it allows the control to modify the mean flow and the fluctuation but does not allow the modification of the fluctuation to feed back onto its mean flow counterpart) is obviously oversimplifying since the mean flow distortion selecting the limit-cycle frequency and amplitude precisely stems from the flow response to the Reynolds stress of the fluctuation. In return, the related theoretical predictions have been shown to lack accuracy in the recirculation region and in the near wake, where the effect of the Reynolds stress is most significant.

An elegant approach to analyze the sensitivity of the shedding frequency has been proposed by Luchini *et al.* (2009), computing first the nonlinear periodic state by DNS, then scaling the time variable on the period of the limit-cycle to bring it out as an explicit unknown, and finally computing the sensitivity by marching adjoint equations backwards in time. Such an approach has the advantage of correctness, but it is computationally very demanding because the adjoint simulation must be run long enough for a time-periodic state to show up and for the adjoint solution to reach statistical equilibrium. Moreover, the DNS solution must be available at all adjoint time-steps, which turns to

be very costly, either in terms of storage resources if one saves all DNS time steps to disk beforehand, or in terms of CPU-time if one saves only a few check-points and recalculates the missing time-steps on the fly. It is proposed here to use the model of Mantič-Lugo *et al.* (2014) to compute self-consistent approximations to this exact sensitivity, which we believe stands as a valuable alternative : first, all sensitivities come at a low computational cost, solving iteratively a couple of equations independent of time. Next, the model is expected to yield improved theoretical predictions at Reynolds numbers not necessarily close to the instability threshold, since it embeds the two-way coupling necessary to describe the mean flow modification induced by the growth of unstable disturbances and the nonlinear saturation of these disturbances as the mean flow becomes neutrally stable. Finally, the approach addresses similarly the sensitivity of the oscillation amplitude. This could be done also with a time-marching adjoint method (to the best of our knowledge, no such results have been reported in the literature) but the detrimental computational costs would then accumulate.

In order to avoid any confusion, we point out that the present research compares three different levels of modeling : linear, semi-linear, and nonlinear (in ascending order, and starting from the lowest level of approximation). On the one hand, *nonlinear* refers to data obtained by DNS of the NSE. On the other hand, *semi-linear* and *linear* refer respectively to data obtained from self-consistent modeling of the NSE, and to their linear approximation computed in the frame of the current sensitivity analysis. The paper is thus organised as follows : in section 2, we recall the main features of the self-consistent theory, and demonstrate its ability to capture accurately the nonlinear limit-cycle frequency and amplitude of controlled cylinder flows of interest. In section 3, we analyze theoretically the sensitivity of the frequency to a steady force in the mean flow equations, and to a synchronous time-harmonic force at the fundamental frequency

in the perturbation equations. The wavemaker region responsible for the selection of the nonlinear frequency is identified from the effect of a localized feedback proportional to the flow velocity. We also consider application to open-loop control by means of a small control cylinder, for which we provide comparison with semi-linear and nonlinear results of the two-cylinder system. Section 4 addresses the sensitivity of the limit-cycle amplitude, and follows the same organization. In concluding the paper, we discuss the ability of the approach to predict complete suppression of vortex shedding.

2. Self-consistent model

We investigate the two-dimensional, incompressible flow past a spanwise infinite circular cylinder of diameter D. We use a Cartesian coordinate system with origin at the cylinder center. We denote by $\mathbf{U} = (U, V)$ the velocity field of components U and V in the streamwise x and cross-stream y directions. P is the pressure, and $\mathbf{x} = (x, y)^T$ is the position vector. Assuming constant kinematic viscosity ν, the sole parameter is the Reynolds number $Re = U_\infty D/\nu$, where U_∞ is the free-stream velocity. The flow is governed by the nonlinear Navier–Stokes equations (NSE) written in compact form as

$$\partial_t \mathbf{U} + \mathbf{N}(\mathbf{U}) = \mathbf{0}\,, \tag{2.1}$$

where $\mathbf{N}(\mathbf{U})$ is the Navier–Stokes operator defined by

$$\mathbf{N}(\mathbf{U}) = \mathbf{U}\cdot\boldsymbol{\nabla}\mathbf{U} + \nabla P - Re^{-1}\boldsymbol{\nabla}^2\mathbf{U}\,, \tag{2.2}$$

whose dependency on P is omitted to ease the notation. For the same reason, we omit the continuity equation $\boldsymbol{\nabla}\cdot\mathbf{U} = 0$, as it is understood that all velocity fields considered in the following must be divergence free because of incompressibility.

2.1. *Description of the model*

The self-consistent theory originates from the Reynolds decomposition of the velocity field into $\mathbf{U}(t) = \mathbf{U}_m + \mathbf{u}'(t)$, where $\mathbf{U}_m = \langle \mathbf{U} \rangle$ is the time-averaged mean velocity and $\mathbf{u}'$ is the fluctuating velocity such that $\langle \mathbf{u}' \rangle = 0$. Introducing $\mathbf{L}(\mathbf{U}_m)$ as the Navier–Stokes operator linearized about the mean flow, substitution into (2.1) yields classical mean flow/fluctuation equations

$$\mathbf{N}(\mathbf{U}_m) = -\left\langle \mathbf{u}' \cdot \boldsymbol{\nabla} \mathbf{u}' \right\rangle , \tag{2.3a}$$

$$\partial_t \mathbf{u}' + \mathbf{L}(\mathbf{U}_m)\mathbf{u}' = -\mathbf{u}' \cdot \boldsymbol{\nabla} \mathbf{u}' + \left\langle \mathbf{u}' \cdot \boldsymbol{\nabla} \mathbf{u}' \right\rangle , \tag{2.3b}$$

defining the mean flow as a solution to the steady NSE, forced by the Reynolds stress of the fluctuation (i.e., the steady part of its nonlinear self-interaction), and the fluctuation as a solution to the NSE linearized about the mean flow, forced by the unsteady part of its nonlinear self-interaction.

In the self-consistent approach, the mean flow is not taken as a given, but comes instead as an output of a semi-linear approximation of (2.3) meant for the perturbation structure to be the one that forces the mean flow by its Reynolds stress in a manner such that the mean flow generates exactly the aforementioned perturbation. Expanding the perturbation into time-harmonic eigenmodes $\mathbf{u}$ of linear growth rate σ and eigenfrequency ω, retaining the dominant eigenmode and forcing its growth rate to zero for the mean flow to be neutrally stable yields

$$\mathbf{N}(\mathbf{U}_m) = -A^2 \boldsymbol{\psi}(\mathbf{u}) , \tag{2.4a}$$

$$(\sigma + \mathrm{i}\omega)\mathbf{u} + \mathbf{L}(\mathbf{U}_m)\mathbf{u} = \mathbf{0} , \tag{2.4b}$$

$$\sigma = 0 , \tag{2.4c}$$

$$||\mathbf{u}|| = 1 , \tag{2.4d}$$

where $||\cdot||$ is the norm induced by the L^2 inner product $(\cdot\,|\,\cdot)$ on the computational domain, A is the real amplitude of the unit-norm eigenmode, $\boldsymbol{\psi}(\mathbf{u}) = 2\Re(\mathbf{u}^* \cdot \boldsymbol{\nabla}\mathbf{u})$ is the Reynolds stress divergence, and $\Re(\cdot)$ and * indicate respectively the real part and the conjugate of a complex quantity. The nonlinearity in $\mathbf{u}$ has been neglected in (2.3b) because vortex shedding is assumed to be dominated by a single harmonic frequency.

This is the key difference with linear stability analyses featuring an eigenvalue problem identical to (2.4b) on behalf of a small-amplitude assumption. If the nonlinearity is neglected in both (2.3a) and (2.3b), the approach is equivalent to classical stability analysis, as the mean flow reduces to the base flow $\mathbf{U}_b$, solution to the steady NSE

$$\mathbf{N}(\mathbf{U}_b) = \mathbf{0}\,, \tag{2.5}$$

computed a priori and supposedly unaffected by the growth of unstable disturbances. Conversely, the approach reduces to mean flow stability analysis if the nonlinearity is neglected only in (2.3b), but taken in account in (2.3a), in which case the mean flow can be computed exactly a priori, averaging in time the instantaneous solution of a direct numerical simulation (DNS) of the NSE. There is however a certain lack of consistency in doing so because the Reynolds stress in (2.3a) is that of the finite-amplitude vortex shedding coming from the DNS, not that of the small-amplitude eigenmode. According to Barkley (2006), the results must be properly interpreted as applying in the case where the Reynolds stress itself is unperturbed at the order of the perturbation, thereby defining the so-called frozen Reynolds stress assumption.

2.2. *Numerical methods*

In the following, we obtain all semi-linear results relaxing the neutral stability condition and increasing the value of A up to the point where $\sigma = 0$ (which we assume is achieved to a sufficient degree when $|\sigma| \leqslant 10^{-6}$). For given amplitude, the self-consistent solutions

are computed iteratively with a finite element method adapted from Meliga *et al.* (2014), to which the reader is referred for further details. At each iteration, the mean flow is computed with the Newton–Raphson method, together with boundary conditions consisting of a uniform free-stream at the inflow, symmetric conditions at the transverse boundaries and a stress-free outflow condition. The perturbation is computed with the Arnoldi method, together with boundary conditions linearized about the mean quantities. This repeats until the difference between two consecutive iterations of $\mathbf{U}_m$ is less than 10^{-12} in L^2 norm, which requires to under-relax the corrections made at each iteration.

In the following, we also report DNS results obtained using a second-order Crank-Nicholson scheme, with time step $\Delta t = 0.05$. At the outflow, a more suitable advective condition is imposed, together with zero pressure at the upper-right corner of the domain. All simulations are carried out until the solution settles down to a periodic state, whereafter it is advanced in time over 500 time units (between 75 and 100 shedding cycles depending on the Reynolds number) sufficiently large to extract accurate frequency and amplitude information.

2.3. *Uncontrolled flow*

In this section, we briefly revisit the self-consistent modeling of the natural (uncontrolled) flow for validation purpose of our numerical tools. For various Reynolds numbers in the range $Re \leqslant 100$, figure 1 reports limit-cycle frequency and amplitude results obtained using a mesh of the computational domain

$$\Omega = \{(x, y) \mid |\mathbf{x}| \geqslant 0.5;\ -30 \leqslant x \leqslant 60;\ |y| \leqslant 25\}\,, \tag{2.6}$$

made of 108,018 triangles (378,660 degrees of freedom), found to offer a good compromise between numerical accuracy and computational effort since numerical tests carried out at two other grid resolutions and spatial extents yield limited variations within 2%. The

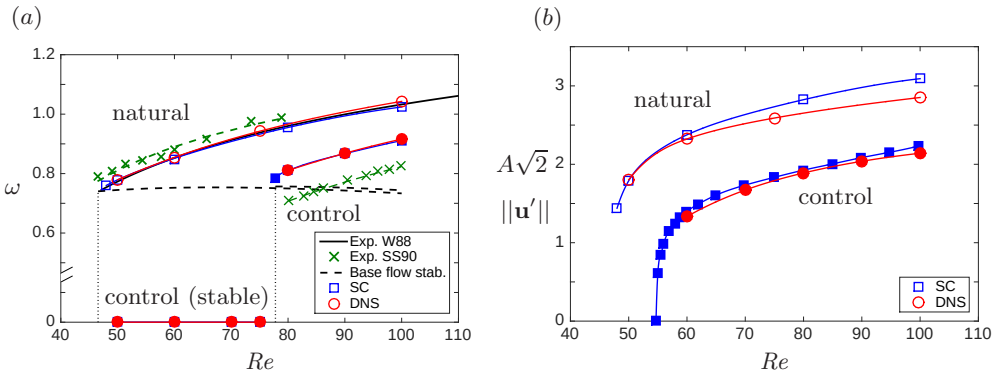

FIGURE 1. Limit-cycle (a) frequency and (b) amplitude as a function of the Reynolds number : self-consistent (blue squares) vs. DNS results (red circles). Open and filled symbols correspond respectively to the natural flow and to control with a secondary cylinder of diameter $d = 0.1$ positioned at (a) $\mathbf{x}_c = (1.2, 1.0)$ and (b) $\mathbf{x}_c = (0.8, 1.6)$. Experimental measurements from Williamson (1988) (black line) and Strykowski & Sreenivasan (1990) (green crosses) are reported for comparison. The dash-dotted lines in (a) correspond to the frequency obtained by linear stability analysis of the base flow.

semi-linear results reported as the open squares exhibit excellent agreement with the nonlinear values extracted from in-house DNS performed on the same mesh, shown as the open circles (note, DNS amplitudes are reported in terms of $\langle||\mathbf{u}'||\rangle$ while self-consistent amplitudes are reported in terms of $A\sqrt{2}$ for the results to be comparable). At $Re = 100$, neutral stability is achieved for $A = 2.2$, or equivalently $A^2||\boldsymbol{\psi}(\mathbf{u})||/||\mathbf{u}||^2 = 0.90$, which matches well the amplitude of Mantič-Lugo *et al.* (2014) obtained normalizing the magnitude of the Reynolds stress instead of that of the eigenmode, and therefore validates the present computations. The associated self-consistent frequency $\omega = 1.02$ ($St = \omega/2\pi = 0.162$) is very consistent with the value 1.03 predicted by the universal Strouhal-Reynolds relationship of Williamson (1988), and with the mean flow stability results of Barkley (2006). The spatial distribution of the self-consistent fields mean flow, fluctuation and Reynolds stress also agrees remarkably well with the DNS results (not shown here for conciseness).

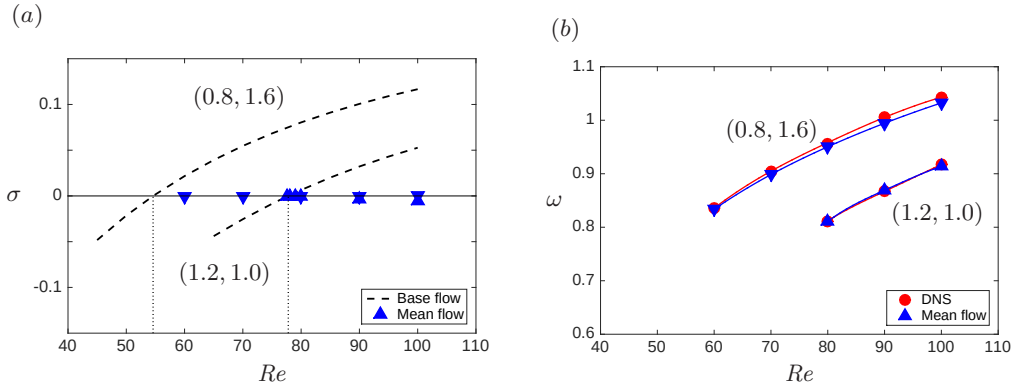

FIGURE 2. (a) Leading growth rate of the time-averaged mean flow as a function of the Reynolds number for control by a cylinder of diameter $d = 0.1$ at $\mathbf{x}_c = (1.2, 1.0)$ (upward triangles) and $\mathbf{x}_c = (0.8, 1.6)$ (downward triangles). The leading growth rate of the base flow is shown for comparison as the dash-dotted lines. (b) Same as (a) for the leading eigenfrequency. The nonlinear frequency extracted from the DNS is indicated by the red circles.

2.4. *Relevance to vortex shedding control*

It is the fundamental premise of our research that the self-consistent theory applies to controlled flows of practical interest. While this is a point that should be addressed on a case-by-case basis for arbitrarily large control amplitudes, we expect that it generally holds true for small to moderate amplitudes. As an illustration, we mimic here the approach of Strykowski & Sreenivasan (1990), insert a control cylinder of diameter $d = 0.1$ at various positions in the flow, and recompute the limit-cycle frequency and amplitude of the two-cylinder system using a mesh of the modified computational domain

$$\Omega_d = \{(x, y) \mid |\mathbf{x}| \geqslant 0.5;\ |\mathbf{x} - \mathbf{x}_c| \geqslant 0.1;\ -30 \leqslant x \leqslant 60;\ |y| \leqslant 25\}\,, \tag{2.7}$$

obtained distributing 300 points at the surface of the control cylinder to accurately represent the flow (Meliga *et al.* 2014). For the positions $\mathbf{x}_c = (1.2, 1.0)$ and $(0.8, 1.6)$ considered, all mean flows are neutrally stable, while the shedding frequency is accurately predicted by the leading eigenfrequency (see figure 2 providing the results of linear stability analysis applied to the time-averaged mean flow), meaning that the controlled

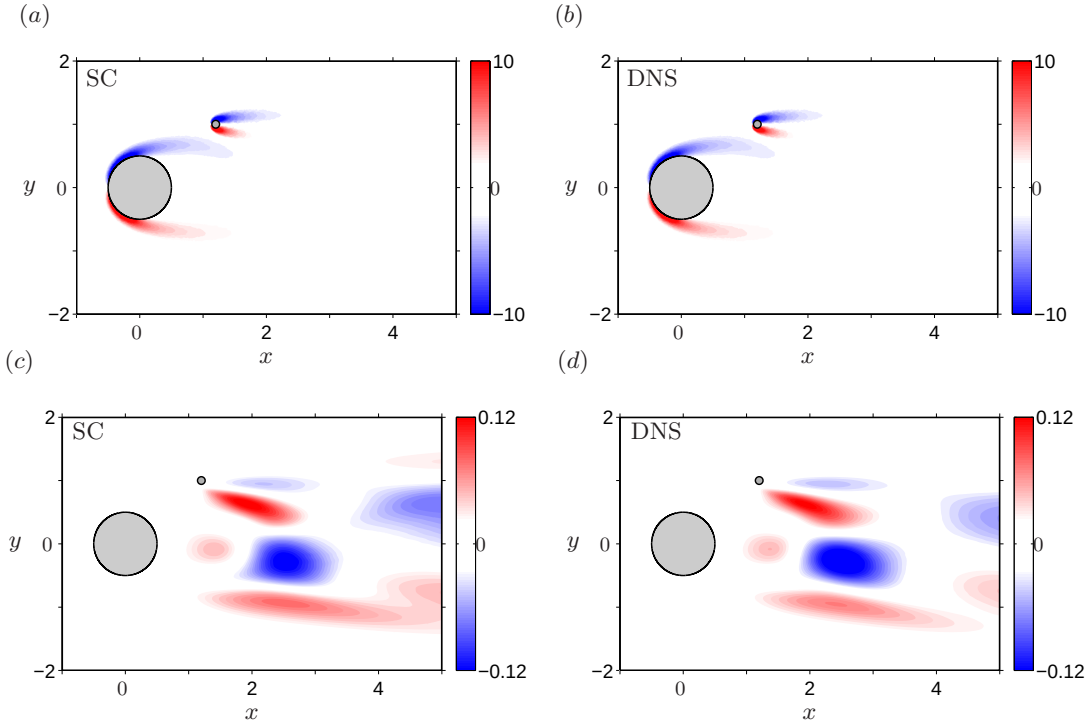

FIGURE 3. (a) Self-consistent vs. (b) time-averaged distribution of mean vorticity for control by a cylinder of diameter $d = 0.1$ at $\mathbf{x}_c = (1.2, 1.0)$ - $Re = 100$. (c)-(d) Same as (a)-(b) for the streamwise component of the Reynolds stress divergence.

flows satisfy the real-zero imaginary-frequency (RZIF) property (Turton *et al.* 2015) and that the self-consistent theory does apply.

The effect on the frequency is illustrated in figure 1(a) for the control cylinder placed at $\mathbf{x}_c = (1.2, 1.0)$. For this case, the critical Reynolds number is $Re_c = 77.8$ (as predicted by linear stability analysis; see figure 2(a)), whereupon the frequency is reduced by approximately 20%. With the above key assumptions fulfilled, the self-consistent approach predicts accurately not only the frequency shift (as seen from the filled squares and circles showing the semi-linear and nonlinear results, respectively), but also the spatial structure of the controlled mean flow and Reynolds stresses, as documented in figure 3. In contrast, the leading eigenfrequency of the base flow (shown as the dashed line in figure 1(a)) is

completely out of range. The self-consistent results are also fully consistent with the experimental data of Strykowski & Sreenivasan (1990) pertaining to the same position of the control cylinder (reproduced as the cross symbols). There does exist a small quantitative difference, that we believe is attributable to a small bias in the experimental results, as the natural frequencies of Strykowski & Sreenivasan (1990) exhibit similar discrepancy with the reference data of Williamson (1988) (shown as the black line). Figure 1(b) illustrates similarly the effect of the control cylinder placed at $\mathbf{x}_c = (0.8, 1.6)$ on the amplitude. For this case, the critical Reynolds number is $Re_c = 55$, whereupon the self-consistent amplitude is reduced by approximately 30%, the agreement between the self-consistent and the DNS results being again excellent.

These results provide clear evidence that the self-consistent theory captures well the effect of the control on the saturation mechanics. As could have been anticipated, different control positions yield markedly different effects on the frequency and the amplitude, for instance a control cylinder at $\mathbf{x}_c = (1.2, 1.0)$ reduces the amplitude twice as less as a control cylinder at $\mathbf{x}_c = (0.8, 1.6)$, while a control cylinder at $\mathbf{x}_c = (0.8, 1.6)$ barely affects the frequency (not shown here). This stresses the need to explore the parameter space for an efficient control design, an investigation from now on performed in a systematic way using sensitivity analysis, as further developed in sections 3 and 4.

3. Sensitivity of the limit-cycle frequency

We assess here the effect of a control in the bulk upon the limit-cycle properties of the self-consistent system

$$\mathbf{N}(\mathbf{U}_m) = -A^2\boldsymbol{\psi}(\mathbf{u}) + \mathbf{F}\,, \tag{3.1a}$$

$$A[(\sigma + \mathrm{i}\omega)\mathbf{u} + \mathbf{L}(\mathbf{U}_m)\mathbf{u}] = \mathbf{f}\,, \tag{3.1b}$$

$$\sigma = 0\,, \tag{3.1c}$$

$$||\mathbf{u}|| = 1\,, \tag{3.1d}$$

where the action of the control is taken into account by a steady body force $\mathbf{F}$ acting as a source term in the mean flow equation (3.1a), and a (complex) harmonic body force $\mathbf{f}$ oscillating at the same frequency as the fundamental eigenmode, and acting as a source term in the perturbation equation (3.1b). From a physical standpoint, $\mathbf{F}$ and $\mathbf{f}$ can be viewed as the mean and fluctuating components of the total (real) body force acting onto the flow, expressed as

$$\mathbf{F} + \mathbf{f}e^{\mathrm{i}\omega t} + \mathbf{f}^* e^{-\mathrm{i}\omega t} = \mathbf{F} + 2\Re(\mathbf{f}e^{\mathrm{i}\omega t})\,. \tag{3.2}$$

This type of forcing is particularly appropriate to model open-loop control by means of a small passive device inserted in the flow, which induces both steady and oscillating forces, as further discussed in the following. Both forces modify the mean flow (directly for the mean component $\mathbf{F}$, indirectly for the fluctuating component $\mathbf{f}$ that changes the Reynolds stress feeding back on the mean flow) and its stability properties. This is rigorously taken into account in the present analysis, with section 4 assessing the change in the amplitude δA needed for the mean flow to return to neutral stability, while the present section addresses the resulting change in the limit-cycle frequency $\delta\omega$.

3.1. *Theoretical framework*

In the limit of infinitesimal control amplitudes, the linear estimate of the limit-cycle frequency variation can be expressed as the inner product between the control forces and sensitivity functions representing the variational derivatives of the frequency to sources of momentum in the flow. This amounts to invoking the first-order Taylor expansion around zero of ω viewed as a function of $\mathbf{F}$ and $\mathbf{f}$, given that only the sensitivity, not the variation, depends on the choice of the inner product structure. We derive here an analytical expression of the sensitivity functions $\boldsymbol{\nabla}_{\mathbf{F}}\omega$ and $\boldsymbol{\nabla}_{\mathbf{f}}\omega$ such that

$$\delta\omega = (\,\boldsymbol{\nabla}_{\mathbf{F}}\omega \,|\, \boldsymbol{\delta}\mathbf{F}) + 2\Re\{(\,\boldsymbol{\nabla}_{\mathbf{f}}\omega \,|\, \boldsymbol{\delta}\mathbf{f})\}\,, \tag{3.3}$$

using a variational technique based on the computation of Lagrange multipliers. We use the body forces $\{\mathbf{F},\mathbf{f}\}$ as control variables, the self-consistent quantities $\{\mathbf{U}_m,\mathbf{u},\sigma,\omega,A\}$ as state (or direct) variables, introduce Lagrange multipliers $\{\mathbf{U}^\dagger,\mathbf{u}^\dagger,\alpha^\dagger,\beta^\dagger\}$ (also termed co-state or adjoint variables) and define the functional

$$\begin{aligned}\mathcal{L}(\mathbf{F},\mathbf{f},\mathbf{U}_m,\mathbf{u},\sigma,\omega,A,\mathbf{U}^\dagger,\mathbf{u}^\dagger,\alpha^\dagger,\beta^\dagger) = \omega &- \left(\mathbf{U}^\dagger \,\middle|\, \mathbf{N}(\mathbf{U}_m) + A^2\boldsymbol{\psi}(\mathbf{u}) - \mathbf{F}\right)\\ &- \left(\mathbf{u}^\dagger \,\middle|\, A[(\sigma+\mathrm{i}\omega)\mathbf{u} + \mathbf{L}(\mathbf{U}_m)\mathbf{u}] - \mathbf{f}\right)\\ &- \left(\mathbf{u}^{\dagger *} \,\middle|\, A[(\sigma-\mathrm{i}\omega)\mathbf{u}^* + \mathbf{L}(\mathbf{U}_m)\mathbf{u}^*] - \mathbf{f}^*\right)\\ &- \alpha^\dagger\sigma - \beta^\dagger\,(1 - (\,\mathbf{u}\,|\,\mathbf{u}))\,,\end{aligned} \tag{3.4}$$

whose gradient with respect to any variable $\mathbf{s}$ is

$$\frac{\partial\mathcal{L}}{\partial\mathbf{s}}\boldsymbol{\delta}\mathbf{s} = \lim_{\epsilon\to 0}\frac{\mathcal{L}(\mathbf{s}+\epsilon\boldsymbol{\delta}\mathbf{s}) - \mathcal{L}(\mathbf{s})}{\epsilon}\,. \tag{3.5}$$

The adjoint fluctuation $\mathbf{u}^\dagger$ is complex, while the adjoint mean flow $\mathbf{U}^\dagger$ and the adjoint scalar parameters $\alpha^\dagger$ (ensuring neutral stability) and $\beta^\dagger$ (ensuring unit norm of the eigenmode) are real, which results in $\mathcal{L}$ being real as well.

Assuming all partial derivatives with respect to the direct and adjoint variables to be zero ($\partial\mathcal{L}/\partial\mathbf{U}_m = \ldots \partial\mathcal{L}/\partial\beta^\dagger = 0$), the total variation of the Lagrangian reads

$$\mathrm{d}\mathcal{L} = \frac{\partial\mathcal{L}}{\partial\mathbf{F}}\boldsymbol{\delta}\mathbf{F} + \frac{\partial\mathcal{L}}{\partial\mathbf{f}}\boldsymbol{\delta}\mathbf{f} + \frac{\partial\mathcal{L}}{\partial\mathbf{f}^*}\boldsymbol{\delta}\mathbf{f}^* = \big(\mathbf{U}^\dagger \,\big|\, \boldsymbol{\delta}\mathbf{F}\big) + 2\Re\big\{\big(\mathbf{u}^\dagger \,\big|\, \boldsymbol{\delta}\mathbf{f}\big)\big\} = \delta\omega\,, \tag{3.6}$$

where the last equality follows from the derivatives with respect to the adjoint variables being zero, which ensures that the direct variables are solutions to the self-consistent system (3.1) and that the Lagrangian reduces to the limit-cycle frequency ($\mathcal{L} = \omega$). Comparing relations (3.3) and (3.6), the sensitivities deduce as

$$\boldsymbol{\nabla}_{\mathbf{F}}\omega = \frac{\partial\mathcal{L}}{\partial\mathbf{F}} = \mathbf{U}^\dagger, \qquad \boldsymbol{\nabla}_{\mathbf{f}}\omega = \frac{\partial\mathcal{L}}{\partial\mathbf{f}} = \mathbf{u}^\dagger\,. \tag{3.7}$$

Using integration by part to cancel the partial derivatives with respect to the direct variables, the adjoint variables come as the solutions to the self-consistent system

$$\mathbf{L}^\dagger(\mathbf{U}_m)\mathbf{U}^\dagger = -2A\,\Re\big(\mathbf{u}^{\dagger *}\cdot\boldsymbol{\nabla}\mathbf{u}^T - \mathbf{u}\cdot\boldsymbol{\nabla}\mathbf{u}^{\dagger *}\big)\,, \tag{3.8a}$$

$$A[(\sigma - \mathrm{i}\omega)\mathbf{u}^\dagger + \mathbf{L}^\dagger(\mathbf{U}_m)\mathbf{u}^\dagger] = -A^2\left(\mathbf{U}^\dagger\cdot\boldsymbol{\nabla}\mathbf{u}^T - \mathbf{u}\cdot\boldsymbol{\nabla}\mathbf{U}^\dagger\right) + 2\beta^\dagger\mathbf{u}\,, \tag{3.8b}$$

$$(\mathbf{u}^\dagger\,|\,\mathbf{u}) = -(\alpha^\dagger + \mathrm{i})/2A\,, \tag{3.8c}$$

$$(\mathbf{U}^\dagger\,|\,\boldsymbol{\psi}(\mathbf{u})) = -\Re\big((\mathbf{u}^\dagger\,|\,\mathbf{f})\big)/A^2\,, \tag{3.8d}$$

where $\mathbf{L}^\dagger$ is the adjoint of the linearized Navier–Stokes operator. At this stage, a compatibility condition must be enforced to guarantee the existence of a solution to the adjoint fluctuation equation (3.8b). This is because there exists a non-trivial solution to

$$(\sigma - \mathrm{i}\omega)\mathbf{u}^\dagger + \mathbf{L}^\dagger(\mathbf{U}_m)\mathbf{u}^\dagger = \mathbf{0}\,, \tag{3.9}$$

for $\sigma = 0$ and ω equal to the limit-cycle frequency, on behalf of $\mathbf{u}$ being a solution to eigenvalue problem (2.4b). Said condition is derived taking the inner product of equation (3.8b) with the eigenmode $\mathbf{u}$ and integrating by parts the left-hand side (LHS),

which yields

$$(\mathbf{u}^\dagger \mid \underbrace{A[(\sigma+\mathrm{i}\omega)\mathbf{u}+\mathbf{L}(\mathbf{U}_m)\mathbf{u})]}_{=\mathbf{f}}) = -A^2\left(\mathbf{U}^\dagger\cdot\boldsymbol{\nabla}\mathbf{u}^T-\mathbf{u}\cdot\boldsymbol{\nabla}\mathbf{U}^\dagger \,\middle|\, \mathbf{u}\right)+2\beta^\dagger\underbrace{(\mathbf{u}\,|\,\mathbf{u})}_{=1}, \quad (3.10)$$

since the operators are by definition such that $\left(\mathbf{u}^\dagger \,\middle|\, \mathbf{L}(\mathbf{U}_m)\mathbf{u}\right) = \left(\mathbf{L}^\dagger(\mathbf{U}_m)\mathbf{u}^\dagger \,\middle|\, \mathbf{u}\right)$. Further integrating by parts the first term in the right-hand side (RHS) and retaining the real part, we obtain

$$\Re\big((\mathbf{u}^\dagger\,|\,\mathbf{f})\big) = -A^2\left(\mathbf{U}^\dagger \,\middle|\, \boldsymbol{\psi}(\mathbf{u})\right)+2\beta^\dagger\,, \quad (3.11)$$

and ultimately

$$\beta^\dagger = 0\,, \quad (3.12)$$

using (3.8*d*). Since we investigate the sensitivity of the natural limit cycle ($\mathbf{f}=\mathbf{0}$), the self-consistent adjoint system reduces to

$$\mathbf{L}^\dagger(\mathbf{U}_m)\mathbf{U}^\dagger = -2A\,\Re\big(\mathbf{u}^{\dagger *}\cdot\boldsymbol{\nabla}\mathbf{u}^T-\mathbf{u}\cdot\boldsymbol{\nabla}\mathbf{u}^{\dagger *}\big)\,, \quad (3.13a)$$

$$A[(\sigma-\mathrm{i}\omega)\mathbf{u}^\dagger+\mathbf{L}^\dagger(\mathbf{U}_m)\mathbf{u}^\dagger] = -A^2\left(\mathbf{U}^\dagger\cdot\boldsymbol{\nabla}\mathbf{u}^T-\mathbf{u}\cdot\boldsymbol{\nabla}\mathbf{U}^\dagger\right)\,, \quad (3.13b)$$

$$(\mathbf{u}^\dagger\,|\,\mathbf{u}) = -(\alpha^\dagger+\mathrm{i})/2A\,, \quad (3.13c)$$

$$(\mathbf{U}^\dagger\,|\,\boldsymbol{\psi}(\mathbf{u})) = 0\,. \quad (3.13d)$$

Both problems (3.13*a*)-(3.13*b*) for the adjoint mean flow and fluctuation must be solved simultaneously, together with normalisation condition (3.13*c*) and compatibility condition (3.13*d*). The boundary conditions are such that the the bilinear concomitant arising on the outer boundary of the domain during the integration by part is zero, which yields classical homogeneous conditions at the inflow, symmetric conditions at the transverse boundaries, and an adjoint stress-free outflow condition (Marquet *et al.* 2008*a*).

Since system (3.13) is independent of time, we obtain the adjoint fields $\mathbf{U}^\dagger$ and $\mathbf{u}^\dagger$ and the adjoint parameter $\alpha^\dagger$ using an iterative method detailed in appendix A.1. Suffice it to say that convergence is achieved within a few tens of iterations, which takes less than an

hour on a regular sequential workstation. The computational cost is thus essentially that of solving the self-consistent system of the uncontrolled flow, which is less than that of performing the DNS on the same mesh in the range of Reynolds number considered herein (by more than 80% at $Re = 60$ and roughly 50% at $Re = 100$). The sensitivity of the limit-cycle frequency to a steady control force ($\boldsymbol{\nabla}_{\mathbf{F}}\omega = \mathbf{U}^\dagger$, physically representing the self-consistent approximation to the mean component of the time-dependent sensitivity computed by Luchini *et al.* (2009)) is presented in figure 4(a) at $Re = 100$. Streamlines of the underlying vector field give the local orientation of the gradient, and color levels indicate its magnitude. In practice, a local steady force $\boldsymbol{\delta}\mathbf{F}$ oriented in the same direction (resp., in the opposite direction) as the arrows plotted in figure 4(a) therefore increases (resp., decreases) the frequency by a quantity proportional to the local magnitude. The regions of highest sensitivity are located on either side of the cylinder, at the periphery of the mean recirculating streamline (shown as the dashed line) and in the inner recirculation region, close to $\mathbf{x} = (1, 0)$. Conversely, the sensitivity to an oscillating control force ($\boldsymbol{\nabla}_{\mathbf{f}}\omega = \mathbf{u}^\dagger$, physically representing the self-consistent approximation to the fluctuating component of the time-dependent sensitivity computed by Luchini *et al.* (2009)) shown in figure 4(b) (with no streamlines since the underlying vector field is complex) is concentrated close to the mean separation points and in the shear layers.

Relation (3.7) carries over to the base and mean flow approaches, provided the adjoint fields are redefined as the solutions to

$$\mathbf{L}^\dagger(\mathbf{U})\mathbf{U}^\dagger = -2\,\Re\big(\mathbf{u}^{\dagger *}\cdot\boldsymbol{\nabla}\mathbf{u}^T - \mathbf{u}\cdot\boldsymbol{\nabla}\mathbf{u}^{\dagger *}\big)\,, \tag{3.14a}$$

$$(\sigma - \mathrm{i}\omega)\mathbf{u}^\dagger + \mathbf{L}^\dagger(\mathbf{U})\mathbf{u}^\dagger = \mathbf{0}\,, \tag{3.14b}$$

$$(\mathbf{u}^\dagger \,|\, \mathbf{u}) = -\mathrm{i}/2\,, \tag{3.14c}$$

with $\mathbf{U}$ being either the base flow or the time-averaged mean flow obtained by DNS.

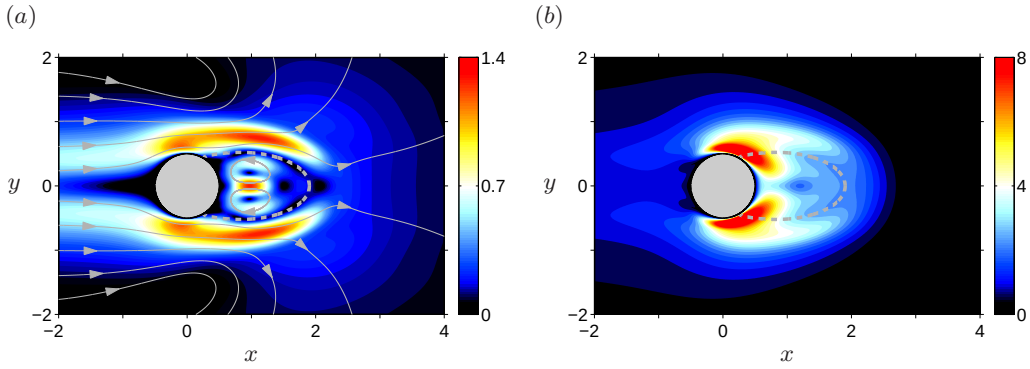

FIGURE 4. Self-consistent sensitivity of the limit-cycle frequency - $Re = 100$. The magnitude of sensitivity is given by the color levels and the orientation of the underlying vector by the superimposed streamlines. (a) Sensitivity to a steady force ($\boldsymbol{\nabla}_{\mathbf{F}}\omega = \mathbf{U}^{\dagger}$). ($b$) Sensitivity to an unsteady force fluctuating at the fundamental frequency ($\boldsymbol{\nabla}_{\mathbf{f}}\omega = \mathbf{u}^{\dagger}$). Note the different color look-up tables in (a) and (b).

System (3.14) is termed *uncoupled* because the eigenvalue problem for the adjoint fluctuation can be solved first, and then the computed solution can be used to solve the adjoint mean flow equation. The sensitivity fields obtained doing so are however markedly different from their self-consistent counterparts, as can be seen comparing figures 4 and 5. Both the base and mean flow approaches somehow end-up providing a rough approximation of the fluctuating component $\boldsymbol{\nabla}_{\mathbf{f}}\omega$, although the base flow approach overestimates the size of the sensitive regions, and the mean flow approach overestimates the level of sensitivity in the vicinity of the separation points. The discrepancy is more obvious looking at the mean component $\boldsymbol{\nabla}_{\mathbf{F}}\omega$, as the base flow approach misses completely on the location and spatial extension of the sensitive regions (not to mention the level of sensitivity in these regions), while the mean flow approach manages to predict, albeit approximately, the location and spatial extension of the primary sensitive regions. Such results clearly stress that an accurate description of the nonlinear mean flow/fluctuation is mandatory to obtain proper sensitivity predictions, as further discussed in section 3.2.

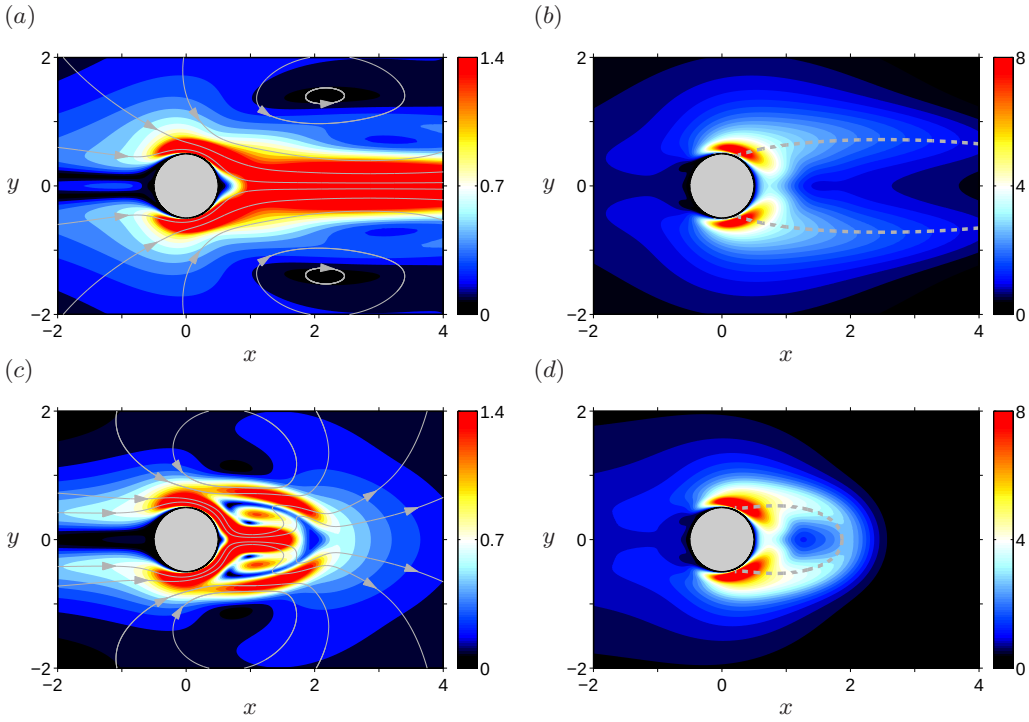

FIGURE 5. Same as figure 4 for the sensitivities computed in the frame of the (a)-(b) base flow approach and of the (c)-(d) mean flow approach - $Re = 100$. The color look-up table is identical to that used in figure 4.

3.2. *Effect of a localized feedback, wavemaker*

In this section, we consider the effect of a 'force-velocity' coupling under the form of a steady force proportional to the mean velocity and a fluctuating force proportional to the eigenmode velocity. If spatially localized, such a forcing can also be viewed as a feedback induced by an actuator located at the same station $\mathbf{x}_c$ as the sensor. Both force components can be expressed as

$$\boldsymbol{\delta}\mathbf{F}(\mathbf{x}) = -b_1\,\mathbf{U}_m(\mathbf{x})\,\delta(\mathbf{x}-\mathbf{x}_c)\,, \tag{3.15}$$

$$\boldsymbol{\delta}\mathbf{f}(\mathbf{x}) = -Ab_2\,\mathbf{u}(\mathbf{x})\,\delta(\mathbf{x}-\mathbf{x}_c)\,, \tag{3.16}$$

where $\delta(\mathbf{x})$ stands for 2D Dirac delta function, $b_{1,2}$ is the amplitude of the feedback, and the frequency variation follows straightforwardly as

$$\delta\omega(\mathbf{x}_c) = -b_1\,\mathbf{U}^\dagger(\mathbf{x}_c)\cdot\mathbf{U}_m(\mathbf{x}_c) - 2Ab_2\Re\big(\mathbf{u}^{\dagger *}(\mathbf{x}_c)\cdot\mathbf{u}(\mathbf{x}_c)\big)\,. \tag{3.17}$$

The Reynolds number is set to $Re = 100$ in the remainder of the section. For several locations of the feedback force, figure 6 compares the linear variation $\delta\omega$ of the limit-cycle frequency computed in the frame of the present self-consistent sensitivity analysis (red lines), whose correctness and numerical accuracy is carefully assessed in appendix A.2, to those obtained by the base and mean flow approaches (dashed and dash-dotted lines). To do so, all delta functions are smoothed out numerically into Gaussians; see Meliga *et al.* (2014) for proof of relevance. For the positions $\mathbf{x}_c = (1.6, 0.5)$ and $\mathbf{x}_c = (1.0, 0.8)$ documented in figure 6(a)-(b), the base flow approach underestimates considerably the frequency variations, which is not too surprising since it even fails to provide a correct estimation of the uncontrolled limit-cycle frequency. The mean flow approach provides a better overall estimation at $\mathbf{x}_c = (1.0, 0.8)$ because the position is not too far downstream, in a region where the mean flow velocity is large and the Reynolds stress is weak. In contrast, at $\mathbf{x}_c = (1.6, 0.5)$ the Reynolds stress is large, and the variation is underestimated by approximately 25%. Looking at the individual variations caused by the mean and fluctuating components of the feedback unveils that both contributions are actually miscalculated but the errors somehow compensate one another (not shown here), meaning the overall comparison is actually worse than it looks. Other comparisons documented in figures 6(c)-(d) add to the proof that overlooking the effect of the control on the Reynolds stress (and its subsequent feedback onto the mean flow) can lead to flawed theoretical predictions, for instance the mean flow approach overestimates the overall variation achieved at $\mathbf{x}_c = (0.0, 0.6)$ by more than 100%, while it squarely fails to predict the sign of that variation achieved at $\mathbf{x}_c = (1.5, 0.0)$.

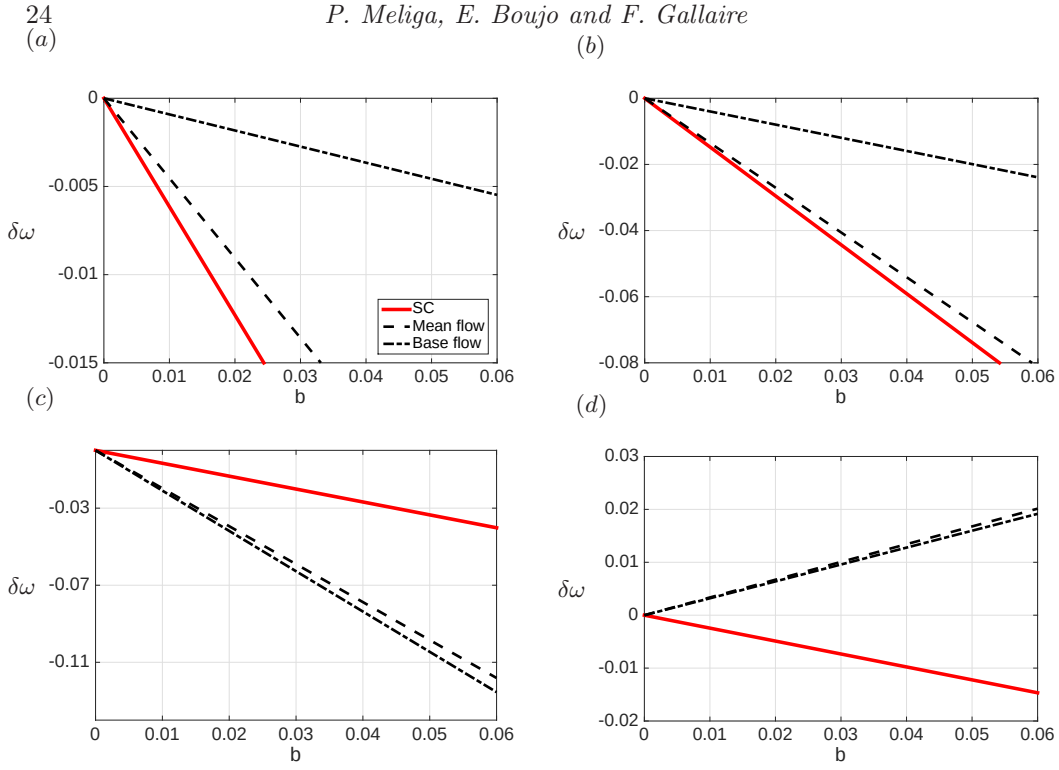

FIGURE 6. Variation of the limit-cycle frequency induced by the localized feedback defined by (3.15) - $Re = 100$. Solid lines indicate linear predictions computed in the frame of the sensitivity analysis from (3.17). The dashed and dash-dotted lines denote the results obtained by the base and the mean flow approaches, respectively. (a) $\mathbf{x}_c = (1.6, 0.5)$. (b) $\mathbf{x}_c = (1.0, 0.8)$. (c) $\mathbf{x}_c = (0.0, 0.6)$. (d) $\mathbf{x}_c = (1.5, 0.0)$.

A bound for the frequency variation induced by the present feedback force can be obtained applying classical Cauchy-Schwartz and triangular inequalities to the RHS of (3.17), which yields

$$|\delta\omega(\mathbf{x}_c)| \leqslant |b_1|\,||\mathbf{U}^\dagger(\mathbf{x}_c)|| \cdot ||\mathbf{U}_m(\mathbf{x}_c)|| + 2A|b_2|\,||\mathbf{u}^\dagger(\mathbf{x}_c)|| \cdot ||\mathbf{u}(\mathbf{x}_c)||\,. \tag{3.18}$$

Equation (3.18) readily expresses that $\delta\omega$ is non-vanishing only in the flow region where the product of the modulus of the self-consistent direct and adjoint fields is not zero. The associated overlapping region can thus be considered as the 'wavemaker' responsible for the selection of the nonlinear frequency, thereby extending the concept introduced

by Giannetti & Luchini (2007) for the leading eigenvalue of the unstable base flow. We show in figure 7(a) the spatial distribution of the product $||\mathbf{U}^\dagger(\mathbf{x}_c)|| \cdot ||\mathbf{U}_m(\mathbf{x}_c)||$ obtained for $(b_1, b_2) = (1, 0)$ and physically representing the contribution of the mean feedback. It is almost zero downstream, but exhibits large magnitudes on either side of the mean recirculation region, and also further upstream, offset from the centerline. In contrast, the magnitude of the product $2A||\mathbf{u}^\dagger(\mathbf{x}_c)||||\mathbf{u}(\mathbf{x}_c)||$ shown in figure 7(b) for $(b_1, b_2) = (0, 1)$ and physically representing the contribution of the fluctuating feedback is almost zero everywhere, except in two lobes located symmetrically across the recirculation region. This is due to the convective non-normality of the NSE transporting in all direct fluctuations downstream and all adjoint fluctuations upstream (Chomaz 2005). Both components of the force therefore sign distinct wavemaker regions, which is consistent with the results of figure 4, but the latter regions differ from those exhibiting only large sensitivity since the amplitude of the direct fields and their orientation with respect to the sensitivities also come into it. Note, a similar wavemaker region has been identified by Luchini *et al.* (2009) from the average in time of the exact product between the time-dependent sensitivity and feedback force, whose self-consistent equivalent is obtained adding up the above products for $|b_1| = |b_2|$. We have checked that almost identical results are obtained doing so, but choose not to discuss further about it because the present results depend on the ratio of $|b_1|/|b_2|$, so the interpretation would somehow lack generality.

3.3. *Application to control by a small circular cylinder*

We now use knowledge of the sensitivity as a systematic guideline on where to insert a small device in the attempt to modify the limit-cycle frequency. This can be of practical interest for fluid-induced vibration problems because the only dangerous flow instabilities are those whose frequencies match the frequencies of the structural eigenmodes, meaning

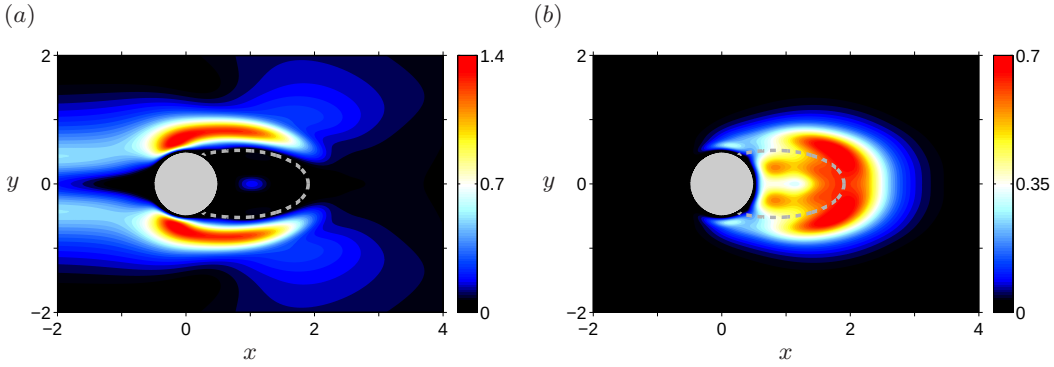

FIGURE 7. Sensitivity of the limit-cycle frequency to a localized feedback as quantified by the products (*a*) $||\mathbf{U}^\dagger(\mathbf{x}_c)|| \cdot ||\mathbf{U}_m(\mathbf{x}_c)||$ and (*b*) $2A||\mathbf{u}^\dagger(\mathbf{x}_c)|| \cdot ||\mathbf{u}(\mathbf{x}_c)||$, representing respectively the contributions of the mean and fluctuating feedback force to the wavemaker.

that shifting the threatening flow frequencies can be sufficient to prevent the onset of synchronized regimes. Following Hill (1992), the presence of a small control cylinder at given position $\mathbf{x}_c$ is modeled by the force it exerts on the flow, defined conveniently as the pointwise reacting force localized at the same location where the control cylinder is placed, equal and opposite to the force that would act on a fictitious cylinder of same diameter invested by a uniform flow at the local velocity. We build here on previous studies focusing on steady and unsteady effects modeling the presence of the control cylinder (Giannetti & Luchini 2007; Marquet *et al.* 2008*a*,*b*; Meliga *et al.* 2010, 2014), and decompose the latter force into steady and fluctuating components reading

$$\boldsymbol{\delta}\mathbf{F}(\mathbf{x}) = -\frac{1}{2}dC_d|\mathbf{U}_m|\mathbf{U}_m\delta(\mathbf{x}-\mathbf{x}_c)\,, \tag{3.19a}$$

$$\boldsymbol{\delta}\mathbf{f}(\mathbf{x}) = -\frac{1}{2}AdC_d\left(|\mathbf{U}_m|\mathbf{u} + \frac{\mathbf{U}_m\cdot\mathbf{u}}{|\mathbf{U}_m|}\mathbf{U}_m\right)\delta(\mathbf{x}-\mathbf{x}_c)\,, \tag{3.19b}$$

where C_d is the drag coefficient of the control cylinder and $|\cdot|$ denotes the norm induced by the dot product. The frequency variation follows straightforwardly as

$$\begin{aligned}\delta\omega(\mathbf{x}_c) = &-\frac{1}{2}dC_d|\mathbf{U}_m(\mathbf{x}_c)|\mathbf{U}^\dagger(\mathbf{x}_c)\cdot\mathbf{U}_m(\mathbf{x}_c) \\ &- AdC_d\Re\left(|\mathbf{U}_m(\mathbf{x}_c)|\mathbf{u}^\dagger(\mathbf{x}_c)\cdot\mathbf{u}(\mathbf{x}_c) + \frac{\mathbf{U}_m(\mathbf{x}_c)\cdot\mathbf{u}(\mathbf{x}_c)}{|\mathbf{U}_m(\mathbf{x}_c)|}\mathbf{u}^\dagger(\mathbf{x}_c)\cdot\mathbf{U}_m(\mathbf{x}_c)\right).\end{aligned} \tag{3.20}$$

Of course, this cylinder force model stands as a first approximation derived in the limit of small control cylinders. On the one hand, it assumes the diameter of the control cylinder to be much smaller than the local inhomogeneity length scale, which results on the force acting on the control cylinder being pure drag (as a non-uniform flow would otherwise exert an additional lift force proportional to the local shear). On the other hand, it assumes negligible inertia effects and thus the force acting on the cylinder at each time instant to be identical to the force that would act if the upstream flow at the same instant was a steady one (quasi-static assumption). This in particular is expected to hold because the advection time scale in the vicinity of the control cylinder is much smaller than the vortex shedding period, a regime where the drag coefficient C_d is essentially equal to its value for steady flow, and thus depends only on the local Reynolds number $Re_d(\mathbf{x}_c) = |\mathbf{U}_m(\mathbf{x}_c)|d/\nu$. The model also assumes the fluctuating force to be harmonic at the fundamental frequency while overlooking the effect of the higher harmonics, which is expected to hold as long as a self-consistent description of the controlled flow remains relevant. We show in the following that even such a basic modeling can guide appropriate placement of the control cylinder in the sense that the localization of the sensitive regions can be safely inferred with good accuracy despite the not-so-high degree of approximation used to represent the control cylinder itself.

We show in figure 8 a map of the variation of the limit-cycle frequency $\delta\omega$ induced by a control cylinder of diameter $d = 0.1$ at $Re = 100$, for which the local Reynolds number is below 10 and the drag coefficient C_d is approximated using the three-parameter power law defined in Meliga *et al.* (2014). It exhibits only negative variations (as indicated by the blue hue) corresponding to a decrease of the frequency, the maximum effect being achieved in a region originating from the shear layers and surrounding the mean recirculating streamline. Weaker yet significant decrease is noticeable further upstream,

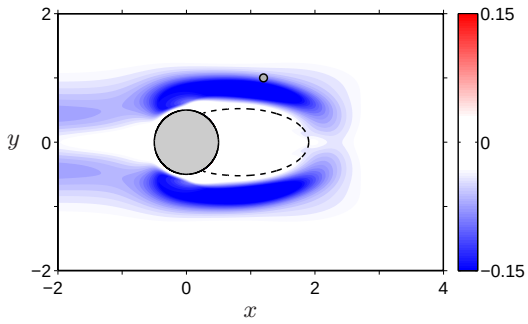

FIGURE 8. Variation of the limit-cycle frequency induced by a control cylinder of diameter $d = 0.1$ whose presence is modeled by equation (3.19) - $Re = 100$. The circle symbol marks the position $\mathbf{x}_c = (1.2, 1.0)$ for which theoretical predictions are compared to self-consistent and DNS results of open-loop control by a small control cylinder in figures 1(a) and 10.

(a) (b)

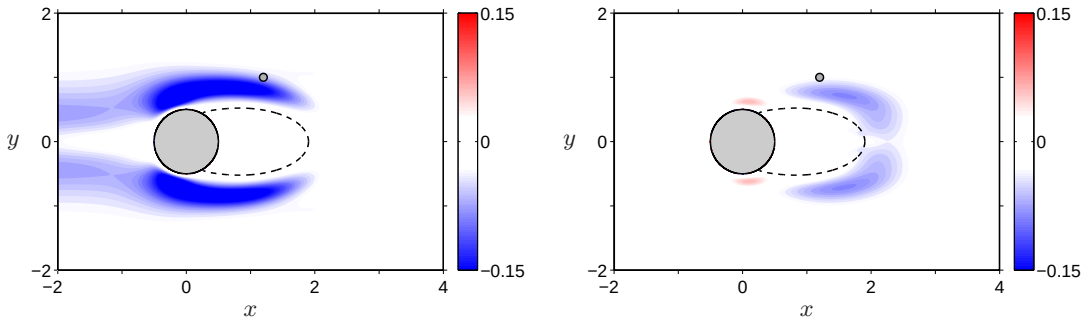

FIGURE 9. Same as figure 8 for the individual variations computed retaining the (a) mean and (b) fluctuating components of the model force. The map in figure 8 is thus retrieved as the sum of these two maps.

offset from the centerline. The maps of the individual variations obtained retaining either the mean or the fluctuating component of the force, shown in figure 9, suggests that it is the mean force (resp. the fluctuating force) that triggers the frequency decrease observed on either side of the mean recirculation region and upstream of the cylinder (resp. in the rear of the recirculation region). The fluctuating force is seen to additionally increase the limit-cycle frequency just upstream of the separation points (red hue), but

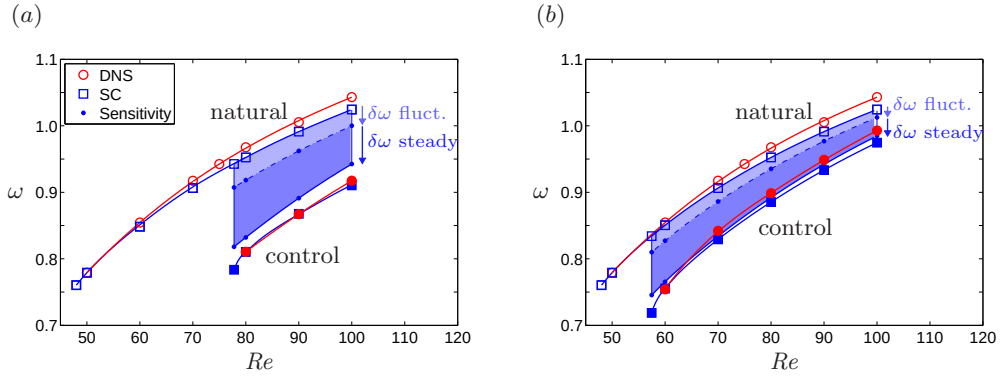

FIGURE 10. Limit-cycle frequency as a function of the Reynolds number for control by a cylinder of diameter (*a*) $d = 0.1$ and (*b*) $d = 0.02$ at $\mathbf{x}_c = (1.2, 1.0)$. Linear sensitivity predictions are shown as the small circle symbols, with dark and light blue shades used to decompose into the contributions of the mean and fluctuating components of the model force. Semi-linear and nonlinear data are also reproduced from figure 1 as the various square/circle symbols.

not sufficiently to compensate for the large decrease induced by the mean force at this location, hence the overall frequency reduction in figure 8. All in all, the mean force produces larger variations, but because of this disjointness in the sensitive regions, the dominant contribution can be driven by either component, depending on the location of the control cylinder.

We return now to the experimental results of Strykowski & Sreenivasan (1990), whom we recall report a control cylinder of diameter $d = 0.1$ placed at at $\mathbf{x}_c = (1.2, 1.0)$ to suppress vortex shedding for $Re < 80$ and to reduce the oscillation frequency by approximately 30% afterwards. In figure 10(*a*), we report the various semi-linear (blue) and nonlinear (red) data used in figure 1(*a*) to evidence that this effect is well captured by the self-consistent theory. We now use blue shades to superimpose the effect of the control cylinder, as theoretically predicted from (3.20), with the dark (resp. light) blue shade representing the effect of the mean (resp. the fluctuating) component of the model force. For this position, marked by the grey circle in figure 8, both components contribute

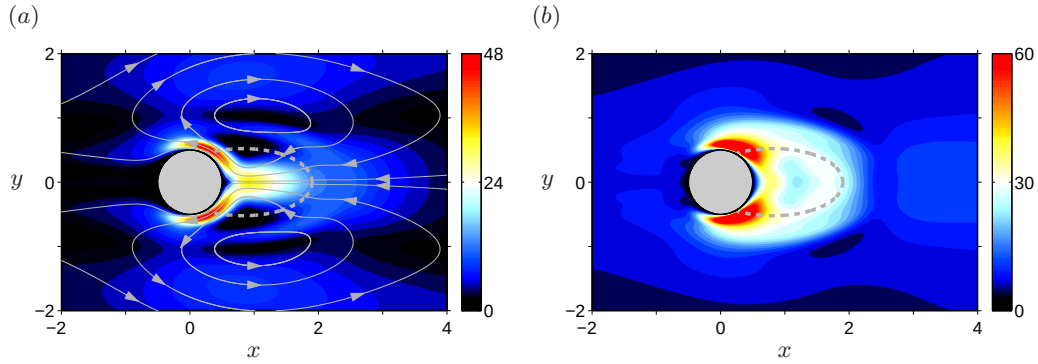

FIGURE 11. Self-consistent sensitivity of the limit-cycle amplitude - $Re = 100$. The magnitude of sensitivity is given by the color levels and the orientation of the underlying vector by the superimposed streamlines. (a) Sensitivity to a steady force ($\boldsymbol{\nabla}_{\mathbf{F}}\omega = \mathbf{U}^{\dagger}$). ($b$) Sensitivity to an unsteady force fluctuating at the fundamental frequency ($\boldsymbol{\nabla}_{\mathbf{f}}\omega = \mathbf{u}^{\dagger}$).

significantly to the frequency reduction, with the variation induced by the mean force being roughly twice as large as that induced by its fluctuating counterpart. The theoretical results exhibit a satisfactory agreement with the semi-linear and nonlinear data, meaning that the approach provides both qualitative and quantitative predictions. There does exist a discrepancy that we attribute to our cylinder force model being excessively simple for such non-small control cylinder, as the agreement is almost perfect in figure 10(b) reporting the same results for a smaller control cylinder of diameter $d = 0.02$.

4. Sensitivity of the limit-cycle amplitude

4.1. *Theoretical framework*

We analyze now similarly the effect of the control upon the limit-cycle amplitude. No comparison is made with the base and mean flow approaches, since those are simply unable to predict the saturation amplitude. In the following, we ease the presentation of the theoretical framework using the squared amplitude A^2 (physically representing the amplitude of the Reynolds stress in the mean flow equation) as convenient direct variable.

An analytical expression of the sensitivity functions $\boldsymbol{\nabla}_{\mathbf{F}}A^2$ and $\boldsymbol{\nabla}_{\mathbf{f}}A^2$, such that

$$\delta A^2 = \big(\boldsymbol{\nabla}_{\mathbf{F}}A^2 \,\big|\, \boldsymbol{\delta}\mathbf{F}\big) + 2\Re\big\{\big(\boldsymbol{\nabla}_{\mathbf{f}}A^2 \,\big|\, \boldsymbol{\delta}\mathbf{f}\big)\big\}\,, \tag{4.1}$$

is derived following the same steps as in section 3.1 to express the total variation of the Lagrangian

$$\begin{aligned}\mathcal{L}(\mathbf{F},\mathbf{f},\mathbf{U}_m,\mathbf{u},\sigma,\omega,A^2,\mathbf{U}^\dagger,\mathbf{u}^\dagger,\alpha^\dagger,\beta^\dagger) = A^2 &- \big(\mathbf{U}^\dagger \,\big|\, \mathbf{N}(\mathbf{U}_m) + A^2\boldsymbol{\psi}(\mathbf{u}) - \mathbf{F}\big)\\ &- \big(\mathbf{u}^\dagger \,\big|\, A[(\sigma+\mathrm{i}\omega)\mathbf{I} + \mathbf{L}(\mathbf{U}_m)\mathbf{u}] - \mathbf{f}\big)\\ &- \big(\mathbf{u}^{\dagger *} \,\big|\, A[(\sigma-\mathrm{i}\omega)\mathbf{I} + \mathbf{L}(\mathbf{U}_m)\mathbf{u}^*] - \mathbf{f}^*\big)\\ &- \alpha^\dagger\sigma - \beta^\dagger(1-(\mathbf{u}\,|\,\mathbf{u}))\,.\end{aligned} \tag{4.2}$$

The sensitivities deduce as

$$\boldsymbol{\nabla}_{\mathbf{F}}A^2 = \frac{\partial\mathcal{L}}{\partial\mathbf{F}} = \mathbf{U}^\dagger, \qquad \boldsymbol{\nabla}_{\mathbf{f}}A^2 = \frac{\partial\mathcal{L}}{\partial\mathbf{f}} = \mathbf{u}^\dagger, \tag{4.3}$$

where the adjoint fields come as solutions to the new self-consistent system

$$\mathbf{L}^\dagger(\mathbf{U}_m)\mathbf{U}^\dagger = -2A\,\Re\big(\mathbf{u}^{\dagger *}\cdot\boldsymbol{\nabla}\mathbf{u}^T - \mathbf{u}\cdot\boldsymbol{\nabla}\mathbf{u}^{\dagger *}\big)\,, \tag{4.4a}$$

$$A[(\sigma-\mathrm{i}\omega)\mathbf{u}^\dagger + \mathbf{L}^\dagger(\mathbf{U}_m)\mathbf{u}^\dagger] = -A^2\left(\mathbf{U}^\dagger\cdot\boldsymbol{\nabla}\mathbf{u}^T - \mathbf{u}\cdot\boldsymbol{\nabla}\mathbf{U}^\dagger\right) + 2\beta^\dagger\mathbf{u}\,, \tag{4.4b}$$

$$(\mathbf{u}^\dagger\,|\,\mathbf{u}) = -\alpha^\dagger/2A\,, \tag{4.4c}$$

$$(\mathbf{U}^\dagger\,|\,\boldsymbol{\psi}(\mathbf{u})) = 1 - \Re\big((\mathbf{u}^\dagger\,|\,\mathbf{f})\big)/A^2\,, \tag{4.4d}$$

formally similar to that (3.13) governing the sensitivity of the limit-cycle frequency, but featuring an additional forcing term in the adjoint fluctuation equation (4.4*b*). Again, a compatibility condition must be enforced to guarantee the existence of a solution, which is achieved taking the inner product of equation (3.8*b*) with the eigenmode $\mathbf{u}$, integrating by parts and retaining the real part. This yields the same relation

$$\Re\big((\mathbf{u}^\dagger\,|\,\mathbf{f})\big) = -A^2\left(\mathbf{U}^\dagger \,\big|\, \boldsymbol{\psi}(\mathbf{u})\right) + 2\beta^\dagger\,, \tag{4.5}$$

as in Section 3.1, except that it reduces now to

$$\beta^\dagger = A^2/2\,, \tag{4.6}$$

using (4.4d). Since we investigate the sensitivity of the natural limit cycle ($\mathbf{f} = \mathbf{0}$), the self-consistent adjoint system ultimately becomes

$$\mathbf{L}^\dagger(\mathbf{U}_m)\mathbf{U}^\dagger = -2A\,\Re\big(\mathbf{u}^{\dagger *}\cdot\boldsymbol{\nabla}\mathbf{u}^T - \mathbf{u}\cdot\boldsymbol{\nabla}\mathbf{u}^{\dagger *}\big)\,, \tag{4.7a}$$

$$A[(\sigma - \mathrm{i}\omega)\mathbf{u}^\dagger + \mathbf{L}^\dagger(\mathbf{U}_m)\mathbf{u}^\dagger] = -A^2\left(\mathbf{U}^\dagger\cdot\boldsymbol{\nabla}\mathbf{u}^T - \mathbf{u}\cdot\boldsymbol{\nabla}\mathbf{U}^\dagger\right) + A^2\mathbf{u}\,, \tag{4.7b}$$

$$(\mathbf{u}^\dagger \,|\, \mathbf{u}) = -\alpha^\dagger/2A\,, \tag{4.7c}$$

$$(\mathbf{U}^\dagger \,|\, \boldsymbol{\psi}(\mathbf{u})) = 1\,. \tag{4.7d}$$

The boundary conditions to be used are those defined in section 3.1, namely homogeneous conditions at the inflow, symmetric conditions at the transverse boundaries, and adjoint stress-free conditions at the outflow.

The numerical method used to compute all adjoint quantities of interest is presented in appendix B.1, together with validation data documented in appendix B.2. The sensitivity of the limit-cycle amplitude to a steady control force ($\boldsymbol{\nabla}_{\mathbf{F}}A^2 = \mathbf{U}^\dagger$) shown in Figure 11($a$) at $Re = 100$ exhibits large magnitudes close to the cylinder, at the mean separating points, as well as in the inner recirculation region, close to the centerline, which constitute noticeable differences with respect to the frequency; see figure 4(a). In contrast, the sensitivity to an oscillating control force ($\boldsymbol{\nabla}_{\mathbf{f}}A^2 = \mathbf{u}^\dagger$) is shown at the same Reynolds number in Figure 11(b) is the largest close to the separation points and (in a lesser extent) in the inner recirculation region, i.e., the same regions where the frequency is most sensitive; see figure 4(b).

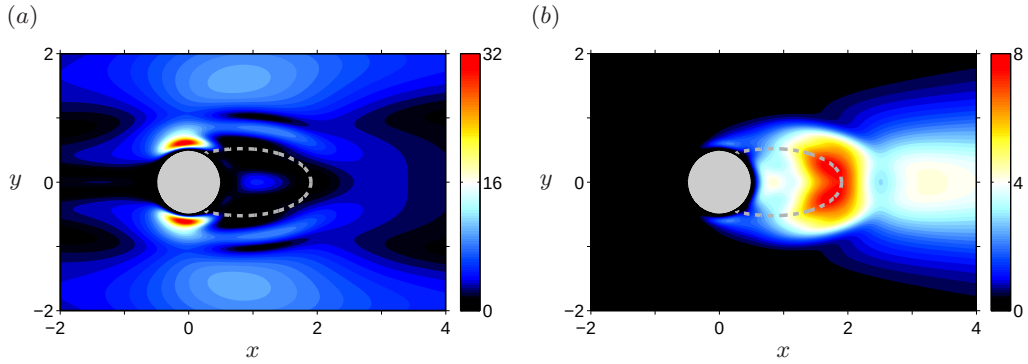

FIGURE 12. Sensitivity of the limit-cycle amplitude to a localized feedback as quantified by the products (a) $||\mathbf{U}^\dagger(\mathbf{x}_c)|| \cdot ||\mathbf{U}_m(\mathbf{x}_c)||$ and (b) $2A||\mathbf{u}^\dagger(\mathbf{x}_c)|| \cdot ||\mathbf{u}(\mathbf{x}_c)||$, representing respectively the contributions of the mean and fluctuating feedback force to the wavemaker - $Re = 100$.

4.2. *Effect of a localized feedback, wavemaker*

We return here to the localized feedback force (3.15) introduced in section 3.2, and present in figure 12 the spatial distribution of the overlapping regions between the self-consistent direct and adjoint fields, considered as the 'wavemaker' of the instability, responsible for the selection of the oscillation amplitude. All results are provided for a Reynolds number $Re = 100$. In figure 12(a), we show the spatial distribution of the product $||\mathbf{U}^\dagger(\mathbf{x}_c)|| \cdot ||\mathbf{U}_m(\mathbf{x}_c)||$ representing the contribution of the mean feedback, whose amplitude is large in the vicinity of the mean separating points, and also moving away from the cylinder surface in the cross-wise direction. In contrast, the magnitude of the product $2A||\mathbf{u}^\dagger(\mathbf{x}_c)|| \cdot ||\mathbf{u}(\mathbf{x}_c)||$ shown in figure 12(b) and representing the contribution of the fluctuating feedback is large in the rear part of the recirculation region, and in the near wake, meaning that both components of the force again sign distinct wavemaker regions.

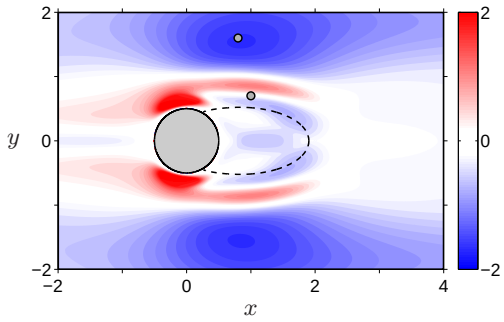

FIGURE 13. Variation of the limit-cycle amplitude induced by a control cylinder of diameter $d = 0.1$ - $Re = 100$. The grey circle mark the positions $\mathbf{x}_c = (0.8, 1.6)$ and $(1.0, 0.7)$ for which theoretical predictions are compared to self-consistent and DNS results of open-loop control by a small control cylinder in figures 1(b) and 15.

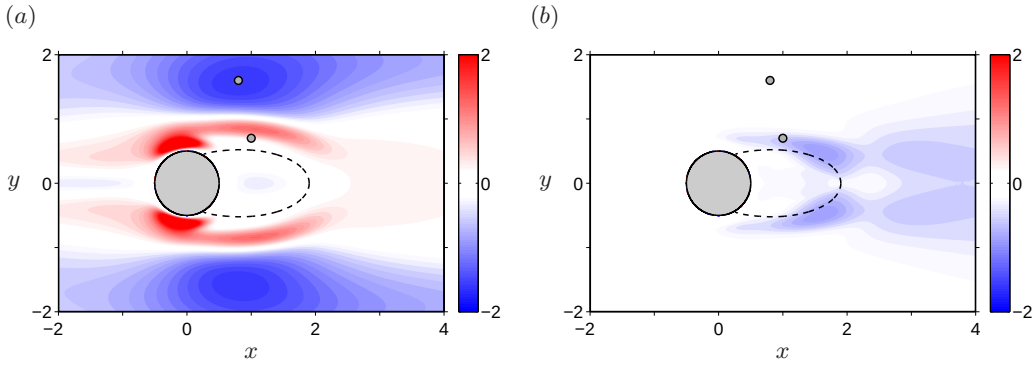

FIGURE 14. Same as figure 13 for the individual variations computed retaining the (a) mean and (b) fluctuating components of the model force.

4.3. *Control by a small circular cylinder*

We use now the sensitivity as a systematic path to guide the best positions for placement of a control cylinder in view of alleviating the shedding activity. We show in figure 13 a map of the variation of the limit-cycle amplitude δA^2 induced by a control cylinder of diameter $d = 0.1$ at $Re = 100$. Interestingly, the control cylinder can increase or decrease the amplitude (while it has been shown to decrease exclusively the frequency in section 3.3), as illustrated by the positive (resp. negative) variations prevailing on either

side of the cylinder and of the mean recirculating streamline (resp. in the rear part of the recirculation and on either side of the recirculation up to the potential flow). Both components of the force act in different flow regions, as seen from figure 14 showing maps of the individual variations obtained retaining either the mean or the fluctuating component of the force. Only the reduction of the amplitude found in the rear part of the recirculation is ascribed to the fluctuating component, while all other variations are essentially driven by the mean force. The fluctuating force also decreases the limit-cycle amplitude in the near-wake region, but this effect is almost exactly counter-balanced by the increase induced by the mean force, hence the absence of any variation in this region in figure 13.

In figure 15(a), we report the various semi-linear and nonlinear data used in figure 1(b) to evidence that the present self-consistent approach predicts well the reduction of the fluctuation amplitude achieved placing a control cylinder of diameter $d = 0.1$ at $\mathbf{x}_c = (0.8, 1.6)$. As in figure 10, we use blue shades to superimpose the effect of the control cylinder as predicted in the frame of the current sensitivity analysis, with the dark (resp. light) blue shade representing the effect of the mean (resp. the fluctuating) component of the model force. For this position, only the dark blue shade is visible, as the contribution of the fluctuating component is negligible, consistently with the results of figure 13. Again, the theoretical results exhibit a good agreement with the semi-linear and nonlinear data, meaning that the approach provides both qualitative and quantitative predictions despite the small discrepancy due to the non-smallness of the control cylinder (see the improved agreement in figure 15(b) showing the exact same results for $d = 0.02$).

Similar results are presented in figure 15(c)-(d) for a control cylinder at $\mathbf{x}_c = (1, 0.7)$, which is a challenging case to be recovered by sensitivity analysis because both components of the force yield significant effects that end up canceling each other out, hence

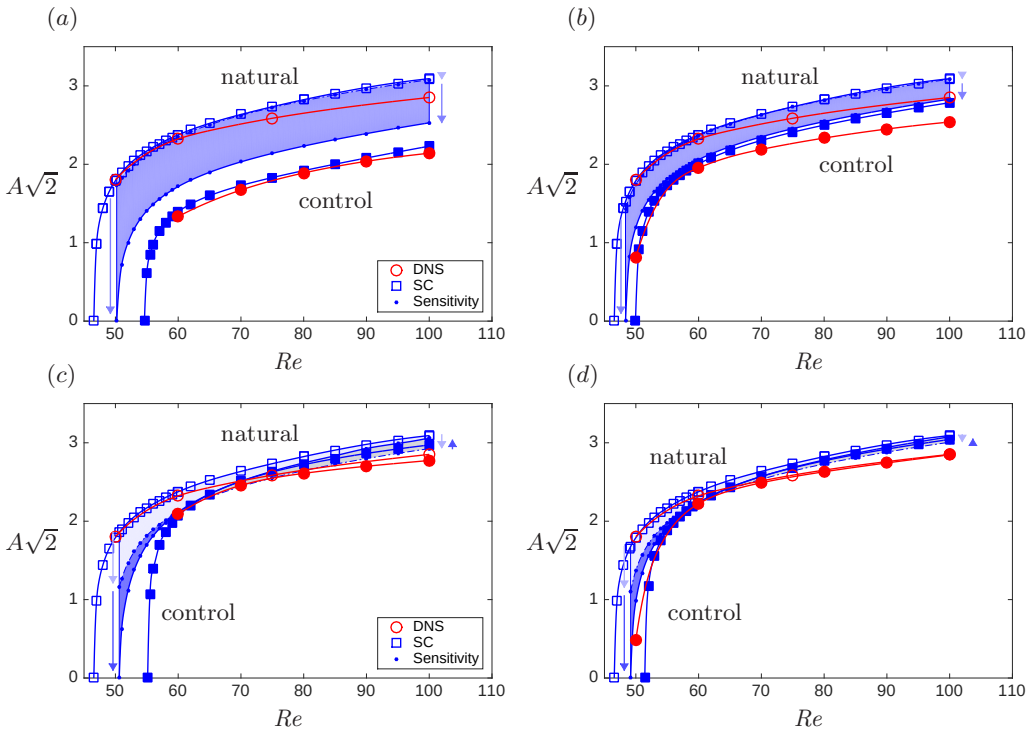

FIGURE 15. (*a*)-(*b*) Limit-cycle amplitude as a function of the Reynolds number for control by a cylinder of diameter (*a*) $d = 0.1$ and (*b*) $d = 0.02$ at $\mathbf{x}_c = (0.8, 1.6)$. Linear sensitivity predictions are shown as the small circle symbols, with dark and light blue shades used to decompose into the contributions of the mean and fluctuating components of the model force. Semi-linear and nonlinear data are also reproduced from figure 1 as the various square/circle symbols. (*c*)-(*d*) Same as (*a*)-(*b*) for a control cylinder at $\mathbf{x}_c = (1.0, 0.7)$.

resulting in little overall variation of the amplitude. Still, we observe a good agreement between the linear and semi-linear results, at least for values of Re not too close to the instability threshold. The discrepancy observed in the vicinity of Re_c however raises interrogations regarding the ability of the approach in identifying those flow regions where the control cylinder completely suppresses vortex shedding. Since the growth rate is forced to zero in the present formulation, it seems natural to correlate such a quenching of the instability to zero limit-cycle amplitude. For a control cylinder of diameter $d = 0.1$, we show in figure 16 the loci of all points in the (x, y)-plane corresponding

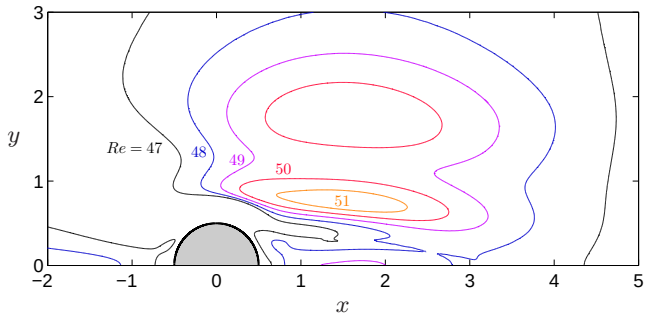

FIGURE 16. Loci of all points in the (x, y)-plane corresponding to zero controlled amplitude for a control cylinder of diameter $d = 0.1$, obtained at several Reynolds numbers from the sensitivity functions as the iso-contours of $\delta A^2 = -A^2$.

to such zero controlled amplitude, calculated at several Reynolds numbers as the iso-contours of $\delta A^2 = -A^2$. In the range $Re < 50$, vortex shedding is suppressed placing the control cylinder either in the outer region or within the recirculation region, close to the centerline. This secondary region vanishes as the Reynolds number increases, while the spatial extent of the outer region reduces until it vanishes as well at $Re = 52$. Such behavior is qualitatively consistent with the results of Strykowski & Sreenivasan (1990) - see the figure 20 herein - but there exist noticeable quantitative differences, since these authors report full restabilization of the flow up to $Re \sim 80$.

Part of the explanation lies in the linear nature of sensitivity methods, whose accuracy is inherently limited by the finite control amplitude needed to stabilize the flow. This can be perilous close to the instability threshold, where the amplitude varies very non-linearly with Re (for such Hopf bifurcation, it varies as the square root of the departure from criticality, opposite to the growth rate which varies linearly). Small inaccuracy in the theoretical model may thus yield non-small discrepancy with the semi-linear results, such miscalculations being clearly visible in figures 15(a) and 15(c), and leading to the related instability thresholds being underestimated by 10% for both positions considered.

Assuming this trend carries over to other positions, this makes the predicted stabilizing regions smaller than they ought to, consistently with the results of figure 16. Another part of the explanation lies in the correlation between suppression of vortex shedding and zero limit-cycle amplitude. Indeed, figure 17(a) pertaining to a control cylinder located at $\mathbf{x}_c = (1.2, 1.0)$ shows that the control affects not only the threshold of instability, but also the structure of the bifurcation, with a small diameter $d = 0.02$ yielding a classical supercritical bifurcation, but the larger diameter $d = 0.1$ yielding an unexpected subcritical bifurcation (which has been assessed rigorously from DNS calculations and from weakly nonlinear analysis, besides the present self-consistent results). This is because the induced mean flow distortion is destabilizing for small amplitudes of the eigenmode amplitude. This is best seen from the evolution of σ as the amplitude A is increased from zero in figure 17(b), where the base flow is initially turned into an increasingly unstable mean flow. For sufficiently large amplitudes $A \gtrsim 0.7$, the nonlinearity becomes stabilizing again and the mean flow is increasingly stabilized, up to the point where neutral stability is achieved. In contrast, for $d = 0.02$, the mean flow distortion is exclusively stabilizing and the growth rate decreases monotonically to zero. Such an effect is local in the sense that for the same diameter $d = 0.1$, the bifurcation remains supercritical at both positions $\mathbf{x}_c = (0.8, 1.6)$ and $(1.0, 0.7)$ documented in figure 15. Even though, the existence of such a fold catastrophe severely impacts the identification of the stabilizing regions because it implies that the limit-cycle amplitude needs not be zero at the critical Reynolds number. Such results suggest that the base flow approach is best suited to predict the suppression of vortex shedding because it allows to correlate the quenching of the instability to zero temporal growth rate (Strykowski & Sreenivasan 1990; Marquet *et al.* 2008*a*). Of course, this is true only if vortex shedding can be suppressed at moderate control amplitudes, otherwise nonlinear effects will alter the predictions in a similar

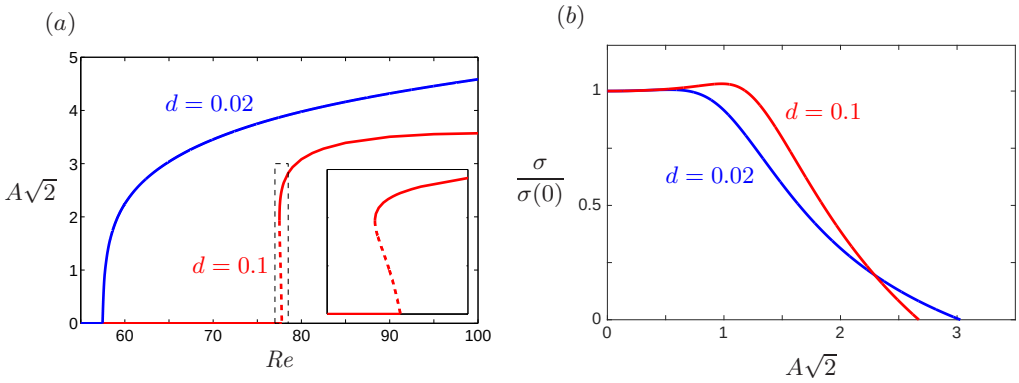

FIGURE 17. (*a*) Limit-cycle amplitude for control by a cylinder at $\mathbf{x}_c = (1.2, 1.0)$. Note the change in the bifurcation structure from supercritical for $d = 0.02$ (blue line) to subcritical - as evidence by the closeup - for $d = 0.1$ (red line). (*b*) Leading growth rate of the mean flow as a function of the amplitude. For both cylinder diameters, the results have been normalized by the growth rate computed for $A = 0$.

fashion. In contrast, the present approach is best suited to guide proper control strategy meant to alleviate finite-amplitude vortex shedding at Reynolds number well above the instability threshold, which constitutes a promising achievement in view of controlling efficiently turbulent flows at practically meaningful high Reynolds numbers.

5. Conclusion

We use the adjoint method to compute sensitivity maps of the limit-cycle frequency and amplitude in the cylinder wake flow above onset of the Bénard-von Kármán vortex street. All calculations are performed in the frame of the semi-linear self-consistent model recently introduced by Mantič-Lugo *et al.* (2014), which allows to describe accurately the effect of the control on the mean flow, but also on the finite-amplitude fluctuation that couples back nonlinearly onto the mean flow via the formation of Reynolds stress. The approach is valid as long as the self-consistent theory applies, which requires the limit-cycle of the controlled flow to be close to harmonic. It provides a valuable alternative

to time-marching adjoint methods such that used by Luchini *et al.* (2009) to derive the sensitivity of the limit-cycle frequency.

The wavemaker regions responsible for the selection of the nonlinear frequency and amplitude are identified from the effect of a localized feedback proportional to the flow velocity. We also apply the method as a systematic guideline to insert a small secondary circular cylinder, whose presence in the flow is modeled by a reacting force localized at the same location where the control cylinder is placed, equal and opposite to the anticipated drag. In doing so, we predict well not only the frequency measured experimentally by Strykowski & Sreenivasan (1990), but also the fluctuation amplitude extracted from in-house DNS calculations. However, the method has difficulty in predicting complete suppression of vortex shedding because non-small control amplitudes can change the underlying bifurcation structure from supercritical to subcritical, which challenges the interpretation of flow stabilization in terms of the self-consistent variables. The approach however serves as a relevant source of information in view of controlling finite-amplitude vortex at Reynolds numbers well above the instability threshold, which cannot be done using the base and mean flow approaches.

It remains to be seen whether the scope of the method can be extended to turbulent flow regimes. The stability analysis of turbulent mean flows is a common practice, see Piot *et al.* (2006); Meliga *et al.* (2009*b*); Hwang & Cossu (2010); Marquillie *et al.* (2011); Iungo *et al.* (2013) among others. The approach generally relies on the triple decomposition of Reynolds & Hussain (1972), so that two levels of mean flow-perturbations are involved. So far, most efforts have focused on the role of the incoherent small-scale turbulence modelled by an eddy viscosity, ranging from simple models in which the eddy viscosity is used only in the mean flow computation (Butler & Farrell 1993) or in the mean flow and the stability computations (del Álamo & Jiménez 2006; Pujals *et al.* 2009; Mettot

et al. 2014) to a fully coupled approach involving the linearisation of the eddy viscosity model (Meliga *et al.* 2012*b*; Viola *et al.* 2014). Concerning the description of the coherent structures, only the mean flow approach has been used so far, i.e. with no feedback of the coherent structures onto the mean flow via the induced Reynolds stress. Promising results have been obtained by doing so, in particular sensitivities have been determined in good qualitative agreement with the experiments (Meliga *et al.* 2012*b*). Still, the present results using the self-consistent approach clearly demonstrate that there remains room for improvement. Because coherent structures are transferring energy to small scales, they are non-monochromatic and whether the present self-consistent model can be generalized to turbulent regimes remains an open issue.

This work is supported by the Investissements d'Avenir French Government program, managed by the French National Research Agency (ANR) through the A*MIDEX grant (ANR-11-IDEX-0001-02) and the LABEX MEC project (ANR-11-LABX-0092).

Appendix A. Sensitivity of the limit-cycle frequency

A.1. *Numerical method*

The self-consistent adjoint system governing the sensitivity of the limit-cycle frequency has been written in section 3.1 as

$$\mathbf{L}^\dagger(\mathbf{U}_m)\mathbf{U}^\dagger = -2A\,\Re\big(\mathbf{u}^{\dagger *}\cdot\boldsymbol{\nabla}\mathbf{u}^T - \mathbf{u}\cdot\boldsymbol{\nabla}\mathbf{u}^{\dagger *}\big)\,, \tag{A 1a}$$

$$A[(\sigma-\mathrm{i}\omega)\mathbf{u}^\dagger + \mathbf{L}^\dagger(\mathbf{U}_m)\mathbf{u}^\dagger] = -A^2\left(\mathbf{U}^\dagger\cdot\boldsymbol{\nabla}\mathbf{u}^T - \mathbf{u}\cdot\boldsymbol{\nabla}\mathbf{U}^\dagger\right)\,, \tag{A 1b}$$

$$(\mathbf{u}^\dagger \,|\, \mathbf{u}) = -(\alpha^\dagger+\mathrm{i})/2A\,, \tag{A 1c}$$

$$(\mathbf{U}^\dagger \,|\, \boldsymbol{\psi}(\mathbf{u})) = 0\,. \tag{A 1d}$$

Before we proceed, it is convenient to start from the *uncoupled* adjoint system

$$\mathbf{L}^\dagger(\mathbf{U}_m)\mathbf{U}^\dagger = -2\,\Re\big(\mathbf{u}^{\dagger *}\cdot\boldsymbol{\nabla}\mathbf{u}^T - \mathbf{u}\cdot\boldsymbol{\nabla}\mathbf{u}^{\dagger *}\big)\,, \tag{A 2a}$$

$$(\sigma - \mathrm{i}\omega)\mathbf{u}^\dagger + \mathbf{L}^\dagger(\mathbf{U}_m)\mathbf{u}^\dagger = \mathbf{0}\,, \tag{A 2b}$$

identical to that showing up in the mean flow approach (except that $\mathbf{U}_m$ denotes here the self-consistent, not time-averaged, mean flow). In the following, we denote by $(\mathbf{U}_i^\dagger, \mathbf{u}_i^\dagger)$ the solution to (A 2) with normalization condition

$$(\mathbf{u}_i^\dagger \,|\, \mathbf{u}) = -\mathrm{i}/2\,, \tag{A 3}$$

physically representing the sensitivities of the frequency ω to steady and fluctuating body force, and by $(\mathbf{U}_r^\dagger, \mathbf{u}_r^\dagger)$ the solution with normalization condition

$$(\mathbf{u}_r^\dagger \,|\, \mathbf{u}) = 1/2\,, \tag{A 4}$$

hence such that $\mathbf{u}_r^\dagger = -\mathrm{i}\mathbf{u}_i^\dagger$, and representing the sensitivities of the growth rate σ.

The self-consistent adjoint fluctuation $\mathbf{u}^\dagger$ is solution to the forced eigenvalue problem (A 1*b*) and can thus be decomposed into the sum of homogeneous and particular solutions according to

$$\mathbf{u}^\dagger = \gamma_r\mathbf{u}_r^\dagger + \gamma_i\mathbf{u}_i^\dagger + \mathbf{u}_p^\dagger = (\gamma_i - \mathrm{i}\gamma_r)\mathbf{u}_i^\dagger + \mathbf{u}_p^\dagger\,, \tag{A 5}$$

where γ_r and γ_i are two (unknown) real coefficients, and the particular solution $\mathbf{u}_p^\dagger$ is by construction such that

$$(\mathbf{u}_p^\dagger \,|\, \mathbf{u}) = 0\,. \tag{A 6}$$

The value of γ_r and γ_i deduces from the normalization condition (A 1*c*) as $\gamma_r = -\alpha^\dagger/A$ and $\gamma_i = 1/A$. Because the adjoint mean flow equation is linear in the adjoint variables, its solution $\mathbf{U}^\dagger$ can be decomposed similarly into

$$\mathbf{U}^\dagger = A\gamma_r\mathbf{U}_r^\dagger + A\gamma_i\mathbf{U}_i^\dagger + \mathbf{U}_p^\dagger = -\alpha^\dagger\mathbf{U}_r^\dagger + \mathbf{U}_i^\dagger + \mathbf{U}_p^\dagger\,, \tag{A 7}$$

where $\mathbf{U}_p^\dagger$ is solution to the forced linear equation

$$\mathbf{L}^\dagger(\mathbf{U}_m)\mathbf{U}_p^\dagger = -2A\,\Re\big(\mathbf{u}_p^{\dagger *}\cdot\boldsymbol{\nabla}\mathbf{u}^T - \mathbf{u}\cdot\boldsymbol{\nabla}\mathbf{u}_p^{\dagger *}\big)\,, \tag{A 8}$$

and the compatibility condition (A 1*d*) imposes that

$$\alpha^\dagger = \frac{(\mathbf{U}_i^\dagger + \mathbf{U}_p^\dagger \,|\, \boldsymbol{\psi}(\mathbf{u}))}{(\mathbf{U}_r^\dagger \,|\, \boldsymbol{\psi}(\mathbf{u}))}\,. \tag{A 9}$$

In practice, solving system (A 1) requires to compute all uncoupled adjoint fields $\mathbf{U}_r^\dagger, \mathbf{u}_r^\dagger, \mathbf{U}_i^\dagger, \mathbf{u}_i^\dagger$ and to initialize $\mathbf{U}^\dagger$ to any guess value. We then compute $\mathbf{u}^\dagger$ solving the adjoint fluctuating equation, deduce the particular solution $\mathbf{u}_p^\dagger$ from the so-obtained numerical solution as

$$\mathbf{u}_p^\dagger = \mathbf{u}^\dagger - \frac{(\mathbf{u}^\dagger \,|\, \mathbf{u})}{(\mathbf{u}_i^\dagger \,|\, \mathbf{u})}\mathbf{u}_i^\dagger\,, \tag{A 10}$$

and compute $\mathbf{U}_p^\dagger$ from equation (A 8). The value of $\alpha^\dagger$ follows from (A 9), which allows to substitute both $\mathbf{u}^\dagger$ and $\mathbf{U}^\dagger$ with their developments (A 5)−(A 7). This repeats until the the difference between two consecutive iterations is less than 10^{-12} in L^2 norm (for both $\mathbf{U}^\dagger$ and $\mathbf{u}^\dagger$), which requires to under-relax the corrections made at each iteration.

A.2. *Validation*

We return to the localized feedback force (3.15) introduced in section 3.2 for validation purposes of our sensitivity calculations. In figure 18, we compare the self-consistent limit-cycle frequency, computed in the frame of the current sensitivity analysis as $\omega + \delta\omega$, to its semi-linear counterpart obtained solving system (3.1) for several values of the feedback amplitude $b_1 = b_2 = b$. Results reported at $Re = 100$ for two feedback locations $\mathbf{x}_c = (1.6, 0.5)$ and $(1.0, 0.8)$ show that the linear sensitivity predictions (red solid lines) and the semi-linear values (red symbols connected by the dashed lines) superimpose one on the other for the smallest feedback amplitudes, which validates the analysis and the accuracy of the computed sensitivity functions since the effect of the control is then linear.

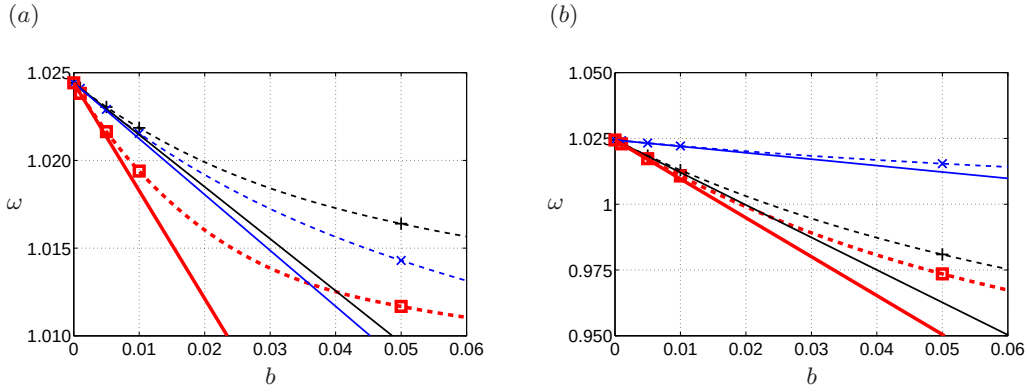

FIGURE 18. Limit-cycle frequency for control by the localized feedback defined by (3.15) - $Re = 100$. The solid lines indicate linear predictions computed in the frame of the present sensitivity analysis from (3.17). The symbols connected by the dashed lines stand for semi-linear values obtained solving the self-consistent system for the controlled flow. The variation induced by the mean and fluctuating feedback forces are shown by the black and blue lines. The total variation is shown by the red lines. (a) $\mathbf{x}_c = (1.6, 0.5)$. ($b$) $\mathbf{x}_c = (1.0, 0.8)$.

The agreement remains satisfying up to moderate feedback amplitudes of order $b \sim 0.01$, whereupon nonlinearities come into play. This results in increasing discrepancies, the effect of the control being systematically overestimated by the sensitivity analysis. We also report in figure 18 the linear sensitivity predictions obtained retaining either the mean (black lines) or the fluctuating (blue lines) feedback, as well as the corresponding semi-linear values obtained solving system (3.1) with either b_2 or b_1 to zero (black/blue symbols). The same excellent agreement is observed for the smallest feedback amplitudes. For both positions, both components of the feedback are cooperative in the sense that they induce variations of the same sign (negative). At $\mathbf{x}_c = (1.6, 0.5)$, the mean and fluctuating components of the feedback contribute almost equally to the total variation (figure 18(a)). Conversely, at $\mathbf{x}_c = (1.0, 0.8)$, the contribution of the fluctuating feedback is much weaker and the total variation is almost entirely due to the mean component (figure 18(b)).

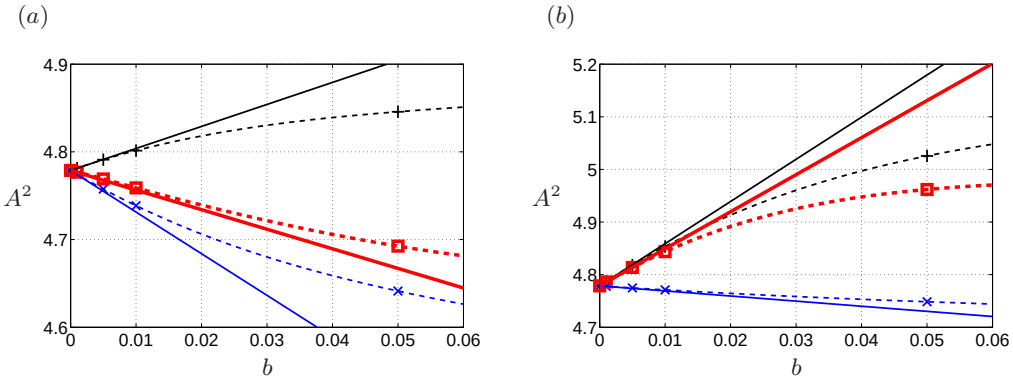

FIGURE 19. Same as figure 18 for the limit-cycle amplitude.

Appendix B. Sensitivity of the limit-cycle amplitude

B.1. *Numerical method*

The self-consistent adjoint system governing the sensitivity of the limit-cycle amplitude has been written in section 4.1 as

$$\mathbf{L}^\dagger(\mathbf{U}_m)\mathbf{U}^\dagger = -2A\,\Re\big(\mathbf{u}^{\dagger *}\cdot\boldsymbol{\nabla}\mathbf{u}^T - \mathbf{u}\cdot\boldsymbol{\nabla}\mathbf{u}^{\dagger *}\big)\,, \tag{B 1a}$$

$$A[(\sigma - \mathrm{i}\omega)\mathbf{u}^\dagger + \mathbf{L}^\dagger(\mathbf{U}_m)\mathbf{u}^\dagger] = -A^2\left(\mathbf{U}^\dagger\cdot\boldsymbol{\nabla}\mathbf{u}^T - \mathbf{u}\cdot\boldsymbol{\nabla}\mathbf{U}^\dagger\right) + A^2\mathbf{u}\,, \tag{B 1b}$$

$$(\mathbf{u}^\dagger \,|\, \mathbf{u}) = -\alpha^\dagger/2A\,, \tag{B 1c}$$

$$(\mathbf{U}^\dagger \,|\, \boldsymbol{\psi}(\mathbf{u})) = 1\,. \tag{B 1d}$$

The method used to solve system (B 1) is identical to that presented in Appendix A.1. The only differences are in the value of the γ_r and γ_i coefficients, now deduced from the normalization condition (B 1*c*) as $\gamma_r = -\alpha^\dagger/A$ and $\gamma_i = 0$, and in the new compatibility condition (B 1*d*) yielding

$$\alpha^\dagger = \frac{-1 + (\mathbf{U}_p^\dagger \,|\, \boldsymbol{\psi}(\mathbf{u}))}{(\mathbf{U}_r^\dagger \,|\, \boldsymbol{\psi}(\mathbf{u}))}\,. \tag{B 2}$$

B.2. *Validation*

In figure 19, we compare the self-consistent limit-cycle amplitude, computed in the frame of the current sensitivity analysis as $A^2 + \delta A^2$, to its semi-linear counterpart obtained

solving system (3.1) for the same feedback amplitudes. Results are reported at $Re = 100$ for the same positions $\mathbf{x}_c = (1.6, 0.5)$ and $\mathbf{x}_c = (1.0, 0.8)$ considered in appendix A.2. The linear sensitivity predictions and the semi-linear values superimpose again one on the other for the smallest feedback amplitudes, which validates the analysis and the accuracy of the computed sensitivities. Similar to the frequency, the sensitivity analysis provides a good estimate of the amplitude in the linear range $b \lesssim 0.01$, whereupon nonlinear effects set in and the variation induced by the control is systematically overestimated. This suggests that nonlinearities tend to cushion the effect of the control on both the frequency and the amplitude. We also show in figure 19 the results obtained retaining either the mean or the fluctuating part of the feedback, which follow the same general behavior. For both positions, these two components are competitive in the sense that they induce variations of opposite signs. At $\mathbf{x}_c = (1.6, 0.5)$, both contributions are of the same order of magnitude, but the overall decrease in the amplitude is due to the effect of the fluctuating feedback being larger (figure 19(a)). Conversely, at $\mathbf{x}_c = (1.0, 0.8)$, the contribution of the fluctuating part is much weaker and the total variation is driven almost entirely by the mean feedback (figure 19(b)).

REFERENCES

del Álamo, J. C. & Jiménez, J. 2006 Linear energy amplification in turbulent channels. *Journal of Fluid Mechanics* **559**, 205–213.

Alizard, F., Robinet, J.-C. & U., Rist 2010 Sensitivity analysis of a streamwise corner flow. *Physics of Fluids* **22**, 014103.

Barkley, D. 2006 Linear analysis of the cylinder wake mean flow. *Europhysics Letters* **75** (5), 750–756.

Boujo, E., Ehrenstein, U. & Gallaire, F. 2013 Open-loop control of noise amplification in a separated boundary layer flow. *Physics of Fluids* **25** (12).

Boujo, E. & Gallaire, F. 2014 Controlled reattachment in separated flows: a variational approach to recirculation length reduction. *Journal of Fluid Mechanics* **742**, 618–635.

Brandt, L., Sipp, D., Pralits, J.O. & Marquet, O. 2011 Effect of base-flow variation in noise amplifiers: the flat-plate boundary layer. *Journal of Fluid Mechanics* **687**, 503–528.

Butler, K.M. & Farrell, B.F. 1993 Optimal perturbations and streak spacing in wall-bounded turbulent shear flow. *Physics of Fluids A: Fluid Dynamics* **5**, 774–777.

Camarri, S., Fallenius, B. E. G. & Fransson, J. H. M. 2013 Stability analysis of experimental flow fields behind a porous cylinder for the investigation of the large-scale wake vortices. *Journal of Fluid Mechanics* **715**, 499–536.

Chomaz, J.M. 2005 Global instabilities in spatially developing flows: Non-normality and nonlinearity. *Annual Review of Fluid Mechanics* **37**, 357–392.

Dušek, J., Le Gal, P. & Fraunié, P. 1994 A numerical and theoretical study of the first Hopf bifurcation in a cylinder wake. *Journal of Fluid Mechanics* **264**, 59–80.

Farrell, B.F. & Ioannou, P.J. 2012 Dynamics of streamwise rolls and streaks in turbulent wall-bounded shear flow. *Journal of Fluid Mechanics* **708**, 149–196.

Giannetti, F. & Luchini, P. 2007 Structural sensitivity of the first instability of the cylinder wake. *Journal of Fluid Mechanics* **581**, 167–197.

Hammond, D. A. & Redekopp, L. G. 1997 Global dynamics of symmetric and asymmetric wakes. *Journal of Fluid Mechanics* **331**, 231–260.

Hill, D. C. 1992 A theoretical approach for analyzing the restabilization of wakes. *AIAA 92-0067* .

Hwang, Y. & Cossu, C. 2010 Amplification of coherent streaks in the turbulent Couette flow: an inputoutput analysis at low Reynolds number. *Journal of Fluid Mechanics* **643**, 333–348.

Iungo, G. V., Viola, F., Camarri, S., Porté-Agel, F. & Gallaire, F. 2013 Linear stability analysis of wind turbine wakes performed on wind tunnel measurements. *Journal of Fluid Mechanics* **737**, 499–526.

Luchini, P., Giannetti, F. & Pralits, J. 2009 Structural sensitivity of the finite-amplitude vortex shedding behind a circular cylinder. In *IUTAM Symposium on Unsteady Separated*

Flows and their Control (ed. M. Braza & K. Hourigan), *IUTAM Bookseries*, vol. 14, pp. 151–160. Springer.

Malkus, W. V. R. 1956 Outline of a theory of turbulent shear flow. *Journal of Fluid Mechanics* **1**, 521–539.

Mantič-Lugo, V., Arratia, C. & Gallaire, F. 2014 Self-consistent mean flow description of the nonlinear saturation of the vortex shedding in the cylinder wake. *Phys. Rev. Lett.* **113**, 084501.

Marquet, O., Sipp, D. & Jacquin, L. 2008*a* Sensitivity analysis and passive control of cylinder flow. *Journal of Fluid Mechanics* **615**, 221–252.

Marquet, O., Sipp, D., Jacquin, L. & Chomaz, J.-M. 2008*b* Multiple scale and sensitivity analysis for the passive control of the cylinder flow. *AIAA 2008-4228* .

Marquillie, M., Ehrenstein, U. & Laval, J.-P. 2011 Instability of streaks in wall turbulence with adverse pressure gradient. *Journal of Fluid Mechanics* **681**, 205–240.

Maurel, A., Pagneux, V. & Wesfreid, J. E. 1995 Mean-flow correction as non-linear saturation mechanism. *EPL (Europhysics Letters)* **32** (3), 217–222.

Meliga, P., Boujo, E., Pujals, G. & Gallaire, F. 2014 Sensitivity of aerodynamic forces in laminar and turbulent flow past a square cylinder. *Physics of Fluids (1994-present)* **26** (10), –.

Meliga, P., Chomaz, J.-M. & Sipp, D. 2009*a* Global mode interaction and pattern selection in the wake of a disk: a weakly nonlinear expansion. *Journal of Fluid Mechanics* **633**, 159–189.

Meliga, P., Gallaire, F. & Chomaz, J.-M. 2012*a* A weakly nonlinear mechanism for mode selection in swirling jets. *Journal of Fluid Mechanics* **699**, 216–262.

Meliga, P., Pujals, G. & Serre, E. 2012*b* Sensitivity of 2-D turbulent flow past a D-shaped cylinder using global stability. *Physics of Fluids (1994-present)* **24** (6).

Meliga, P., Sipp, D. & Chomaz, J.-M. 2009*b* Elephant modes and low frequency unsteadiness in a high Reynolds number, transonic afterbody wake. *Physics of Fluids (1994-present)* **21** (5), –.

Meliga, P., Sipp, D. & Chomaz, J.-M. 2010 Open-loop control of compressible afterbody flows using adjoint methods. *Physics of Fluids* **22** (5), 054109.

Mettot, C., Sipp, D. & Bézard, H. 2014 Quasi-laminar stability and sensitivity analyses for turbulent flows: Prediction of low-frequency unsteadiness and passive control. *Physics of Fluids (1994-present)* **26** (4), –.

Noack, B. R., Afanasiev, K., Morzynski, M., Tadmor, G. & Thiele, F. 2003 A hierarchy of low-dimensional models for the transient and post-transient cylinder wake. *Journal of Fluid Mechanics* **497**, 335–363.

Pier, B. 2002 On the frequency selection of finite-amplitude vortex shedding in the cylinder wake. *Journal of Fluid Mechanics* **458**, 407–417.

Piot, E., Casalis, G., Muller, F. & Bailly, C. 2006 Investigation of the PSE approach for subsonic and supersonic hot jets. Detailed comparisons with LES and Linearized Euler Equations results. *International Journal of Aeroacoustics* **5** (4), 361–393.

Pralits, J.O., Bottaro, A. & S., Cherubini 2015 Weakly nonlinear optimal perturbations. *Journal of Fluid Mechanics* **785**, 135–151.

Pralits, J.O., Brandt, L. & Giannetti, F. 2010 Instability and sensitivity of the flow around a rotating circular cylinder. *Journal of Fluid Mechanics* **650**, 513–536.

Pujals, G., García-Villalba, M., Cossu, C. & Depardon, S. 2009 A note on optimal transient growth in turbulent channel flows. *Physics of Fluids (1994-present)* **21** (1), –.

Reynolds, W. C. & Hussain, A. K. M. F. 1972 The mechanics of an organized wave in turbulent shear flow. Part 3. Theoretical models and comparisons with experiments. *Journal of Fluid Mechanics* **54**, 263–288.

Sipp, D. & Lebedev, A. 2007 Global stability of base and mean flows: a general approach and its applications to cylinder and open cavity flows. *Journal of Fluid Mechanics* **593**, 333–358.

Strykowski, P. J. & Sreenivasan, K. R. 1990 On the formation and suppression of vortex 'shedding' at low Reynolds numbers. *Journal of Fluid Mechanics* **218**, 71–107.

Stuart, J. T. 1960 On the non-linear mechanics of wave disturbances in stable and unsta-

ble parallel flows Part 1. The basic behaviour in plane Poiseuille flow. *Journal of Fluid Mechanics* **9**, 353–370.

Turton, S.E., Tuckerman, L.S. & Barkley, D. 2015 Prediction of frequencies in thermosolutal convection from mean flows. *Physical Review E* **91**, 043009.

Viola, F., Iungo, G. V., Camarri, S., Porté-Agel, F. & Gallaire, F. 2014 Prediction of the hub vortex instability in a wind turbine wake: stability analysis with eddy-viscosity models calibrated on wind tunnel data. *Journal of Fluid Mechanics* **750**.

Williamson, C. H. K. 1988 Defining a universal and continuous Strouhal-Reynolds number relationship for the laminar vortex shedding of a circular cylinder. *Physics of Fluids (1958-1988)* **31** (10), 2742–2744.

Williamson, C. H. K. 1996 Vortex dynamics in the cylinder wake. *Annual Review of Fluid Mechanics* **28**, 477–539.

Zielinska, B. J. A., Goujon-Durand, S., Dušek, J. & Wesfreid, J. E. 1997 Strongly nonlinear effect in unstable wakes. *Phys. Rev. Lett.* **79**, 3893–3896.